Supplementary Information

Ten Thousand Hour Stable Zinc Air Batteries via Fe and W Dual Atom Sites

Yifan Li[1], Hanlin Wang[1], Chang Chen[2], Xuesong Xie[1], Yang Yang[1], Xuehai Tan[1], Keren Jiang[1], Ning Chen[3], Hao Zhang[1]*, Zhi Li[1]*

[1]*Department of Chemical and Materials Engineering, University of Alberta, Edmonton, Alberta T6G 1H9, Canada*

[2]*Engineering Research Center of Advanced Rare Earth Materials, Department of Chemistry, Tsinghua University, Beijing, 100000, China*

[3]*Hard X-Ray Micro Analysis BL, Canadian Light Source Saskatoon, Saskatchewan, S7N 2V3 Canada*

Contents:

Supplementary Figures

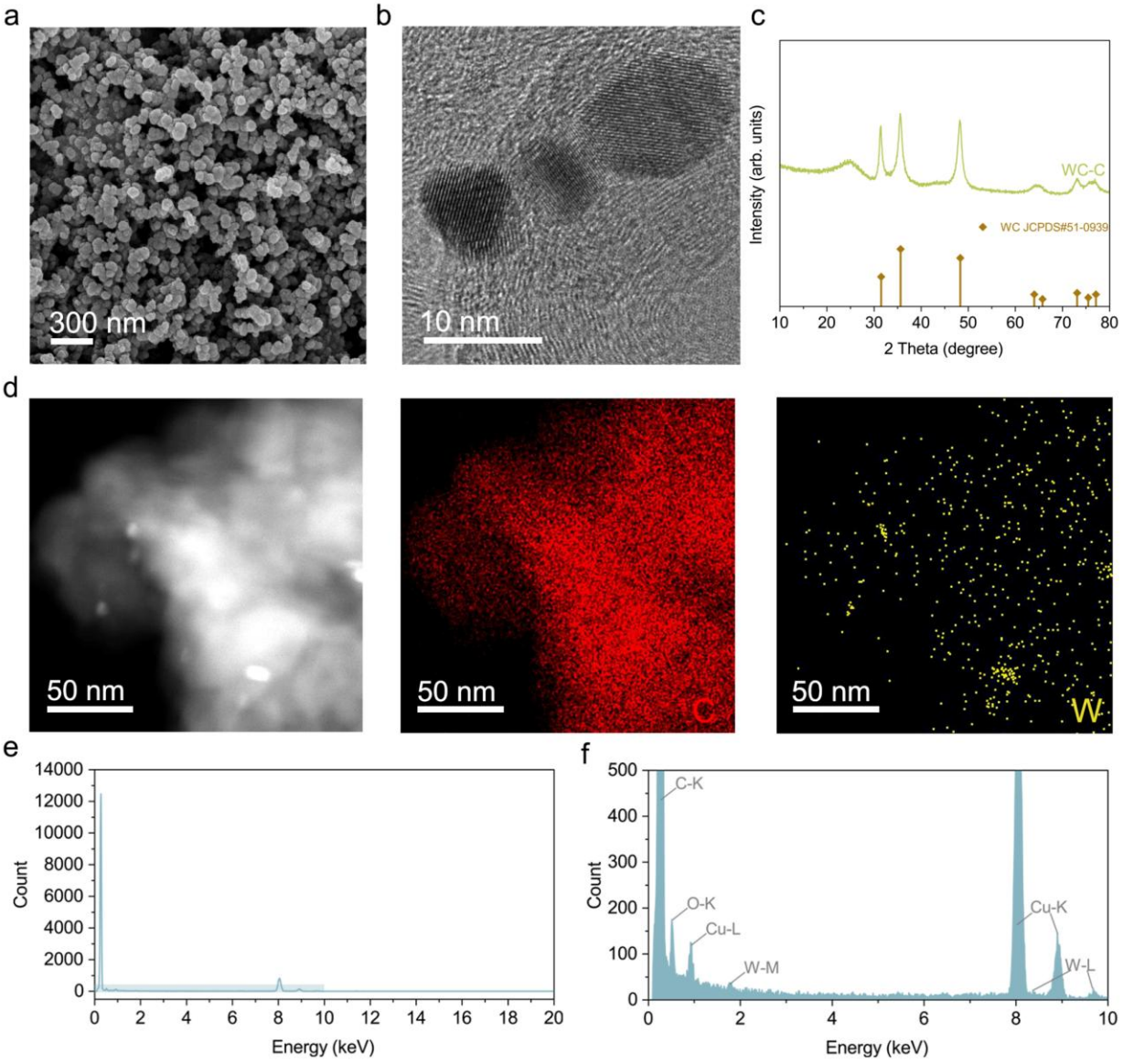

Supplementary Fig. 1. Morphological characterizations of WC-C catalyst. **a**, Scanning electron microscopy (SEM) image. **b**, Transmission electron microscopy (TEM) image. **c**, X-ray diffraction (XRD) pattern. **d**, High-angle annular dark-field scanning transmission electron microscopy (HAADF-STEM) image and corresponding energy-dispersive X-ray spectroscopy (EDX) mapping images for C (red) and W (yellow). **e**, Corresponding EDX spectrum. **f**. Enlarged EDX spectrum corresponding to the shaded area in (e).

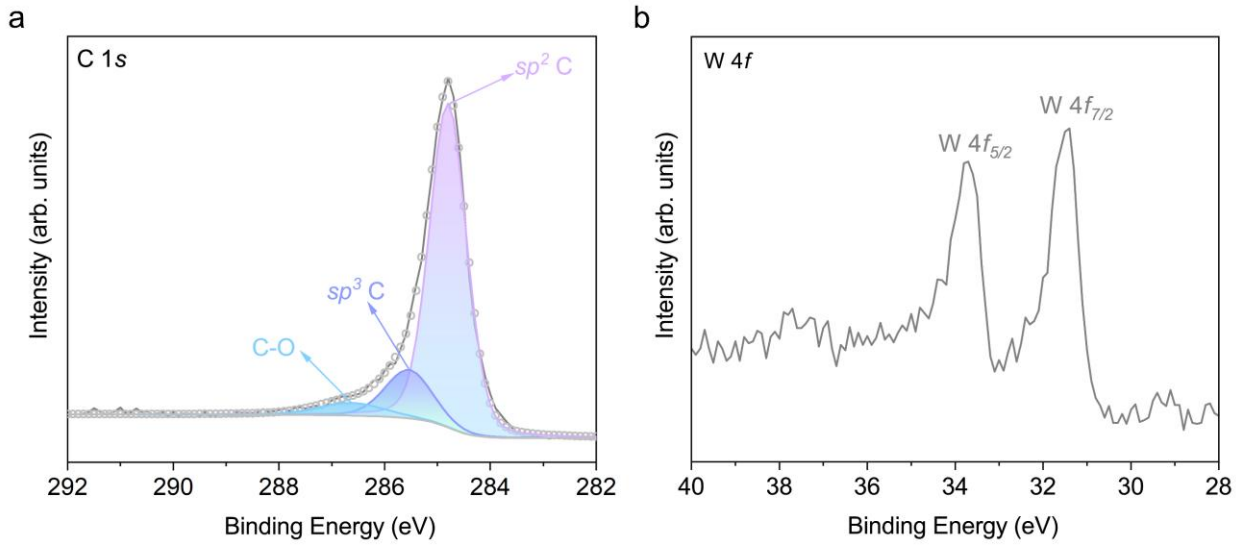

Supplementary Fig. 2. X-ray photoelectron spectroscopy (XPS) analysis of WC-C catalyst. **a**, High-resolution XPS spectrum of C 1*s*. **b**, High-resolution XPS spectrum of W 4*f*.

Notably, the WC-C catalyst exhibits W $4f_{5/2}$ and W $4f_{7/2}$ peaks at binding energies of 33.7 and 31.4 eV. The $4f_{7/2}$ binding energy of W is about 0.8 eV higher than that of metallic W (30.6 eV), and the chemical shift of W 4*f* peaks attributed to the charge transfer from tungsten to carbon atoms upon WC compound formation[1-3].

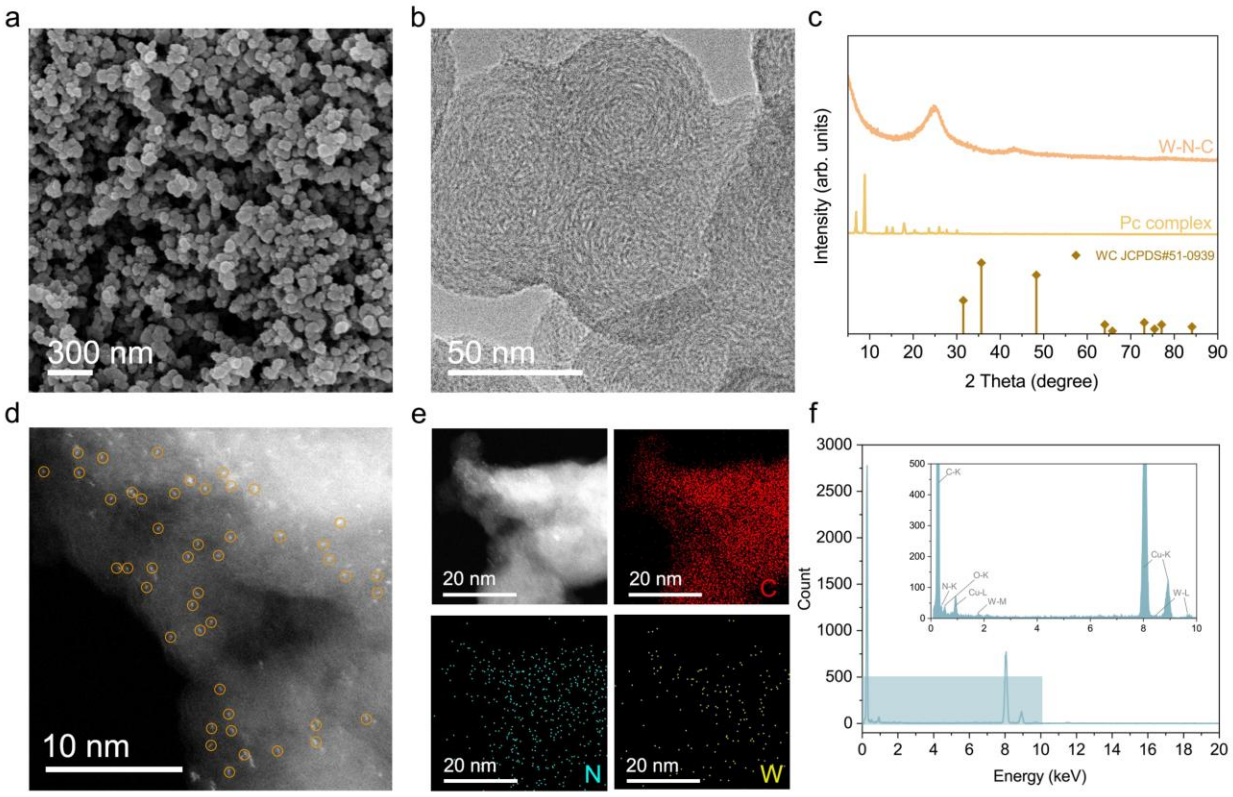

Supplementary Fig. 3. Morphological characterizations of W-N-C catalyst. **a**, SEM image. **b**, TEM image. **c**, XRD patterns of W-N-C catalyst and phthalocyanine crystalline complex (Pc complex). **d**, Aberration-corrected HAADF-STEM image. **e**, HAADF-STEM image and corresponding EDX mapping images for C (red), N (blue) and W (yellow). **f**, Corresponding EDX spectrum, and the inset is the enlarged EDX spectrum of the shaded area.

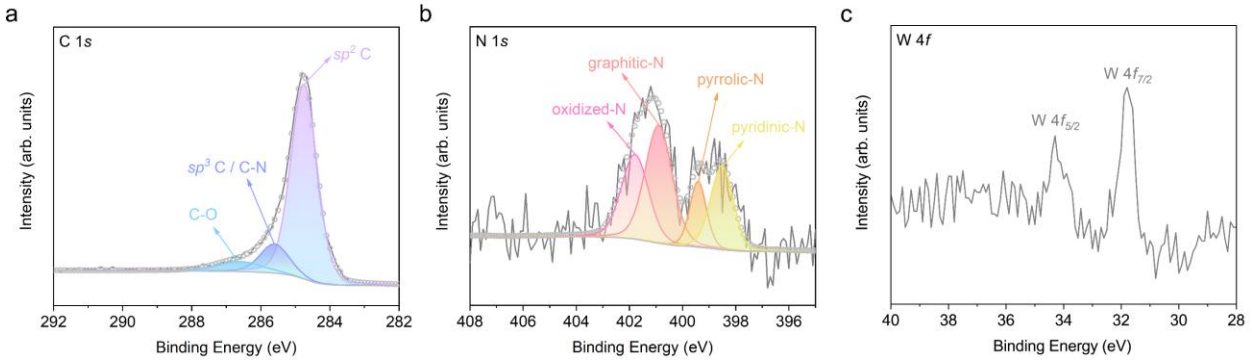

Supplementary Fig. 4. XPS analysis of W-N-C catalyst. **a**, High-resolution XPS spectrum of C 1*s*. **b**, High-resolution XPS spectrum of N 1*s*. **c**, High-resolution XPS spectrum of W 4*f*.

Notably, the W-N-C catalyst exhibits W $4f_{5/2}$ and W $4f_{7/2}$ peaks at binding energies of 34.3 and 31.8 eV. This could be attributed to the introduction of N atoms during the ball milling process, which forms W-N coordination on the carbon black surface. Since N has a stronger electronegativity than C, a larger chemical shift is generated by comparing with the WC-C catalyst[4]. Moreover, the binding energy of W $4f_{7/2}$ in W-N-C catalyst is significantly lower than that of WO_2 (32.9 eV) and WO_3 (35.6 eV), proving the existence of W-N coordination[4,5].

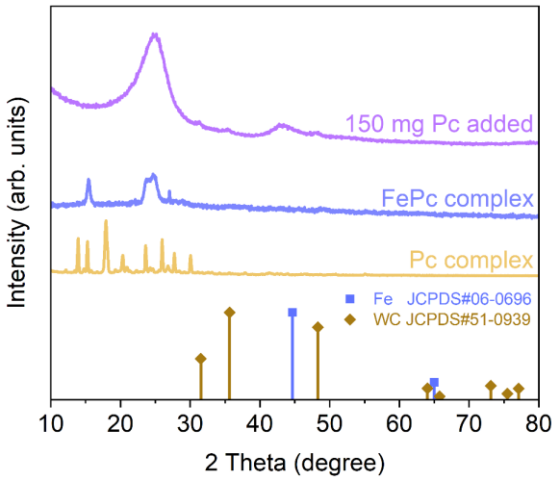

Supplementary Fig. 5. XRD patterns of Pc complex, FePc complex, and the catalyst prepared by adding 150 mg Pc during the ball milling process.

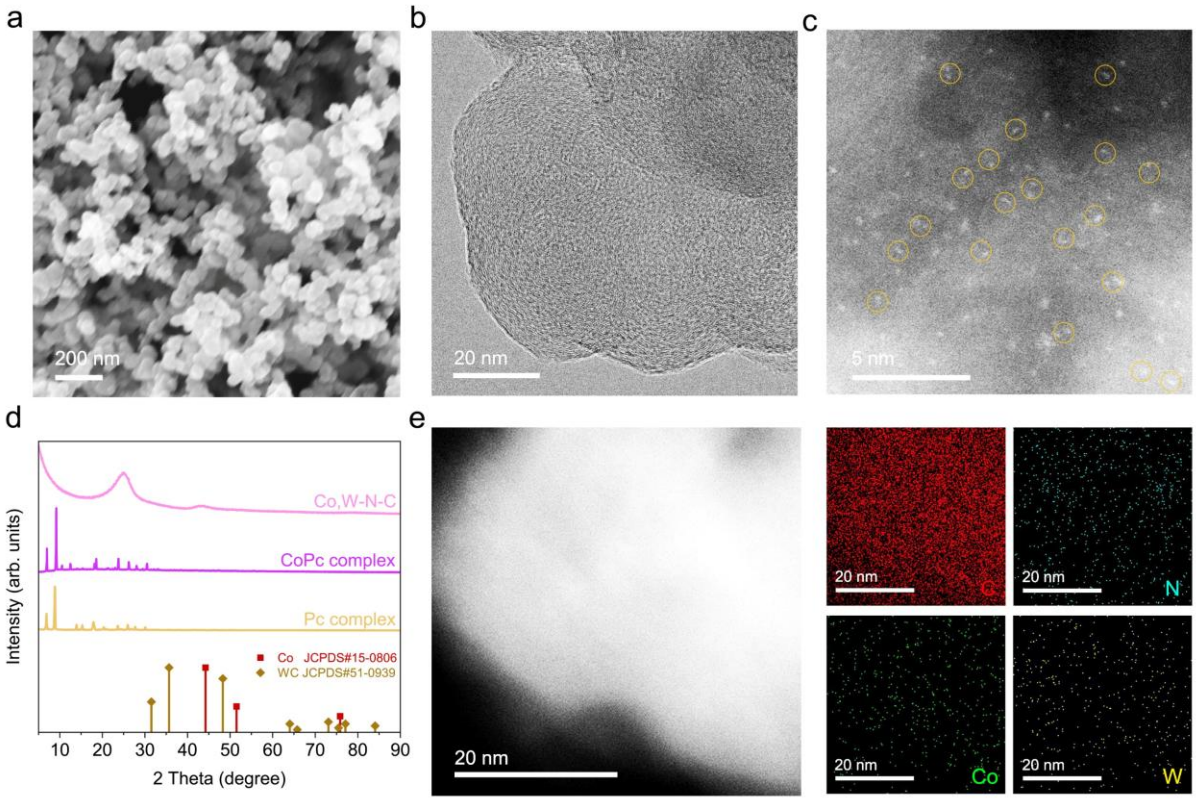

Supplementary Fig. 6. Morphological characterizations of Co,W-N-C catalyst. **a**, SEM image. **b**, TEM image. **c**, Aberration-corrected HAADF-STEM image. **d**, XRD patterns of Co,W-N-C catalyst, cobalt (II) phthalocyanine complex (CoPc complex) and Pc complex. **e**, HAADF-STEM image and corresponding EDX mapping images for C (red), N (blue), Co (green) and W (yellow).

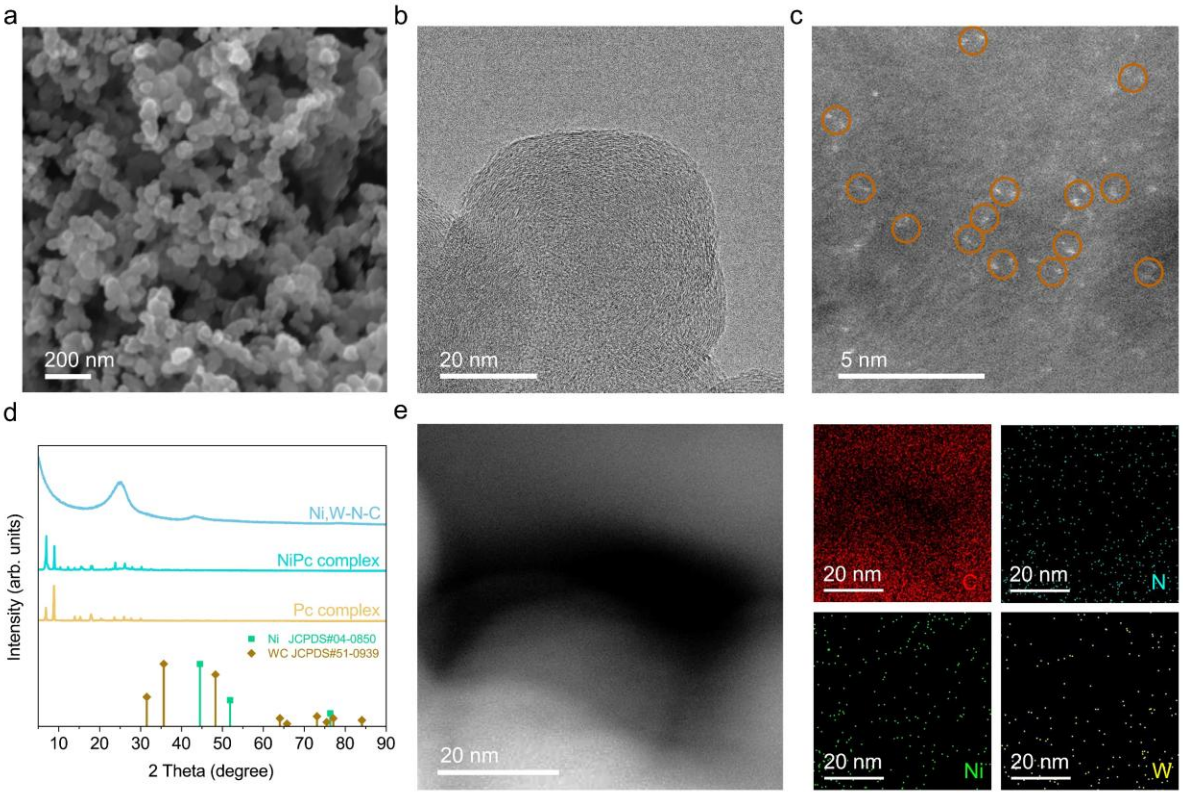

Supplementary Fig. 7. Morphological characterizations of Ni,W-N-C catalyst. **a**, SEM image. **b**, TEM image. **c**, Aberration-corrected HAADF-STEM image. **d**, XRD patterns of Ni,W-N-C catalyst, nickel phthalocyanine complex (NiPc complex) and Pc complex. **e**, HAADF-STEM image and corresponding EDX mapping images for C (red), N (blue), Ni (green) and W (yellow).

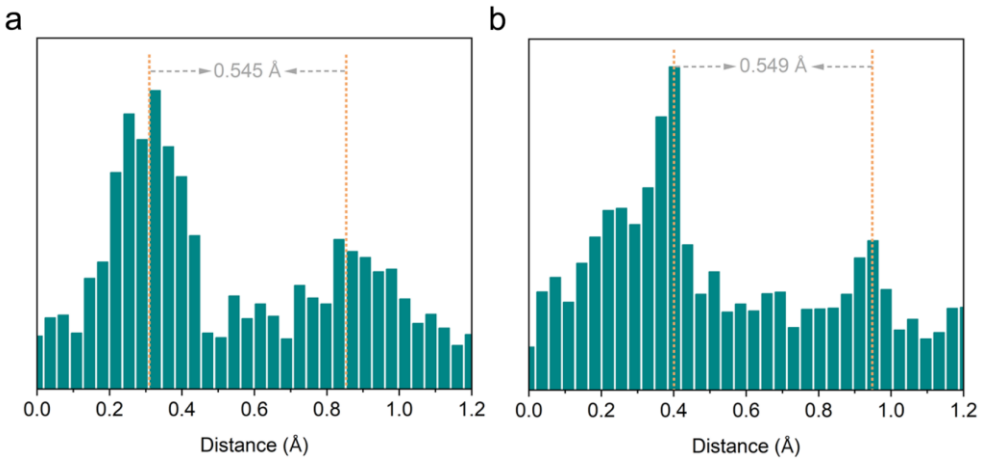

Supplementary Fig. 8. Distance between two adjacent metal atoms in site 1 (**a**) and site 2 (**b**).

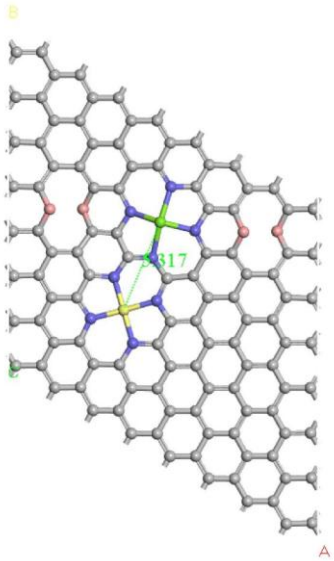

Supplementary Fig. 9. Atomic configuration of the Fe,W-N-C catalyst.

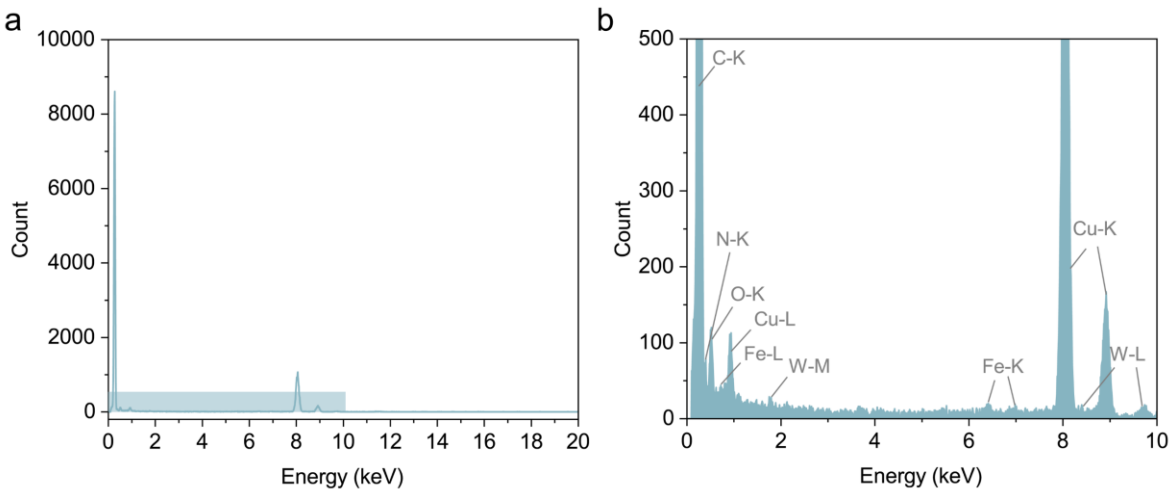

Supplementary Fig. 10. a, Corresponding EDX spectrum of the Fe,W-N-C catalyst. **b**, Enlarged EDX spectrum corresponding to the shaded area in (a).

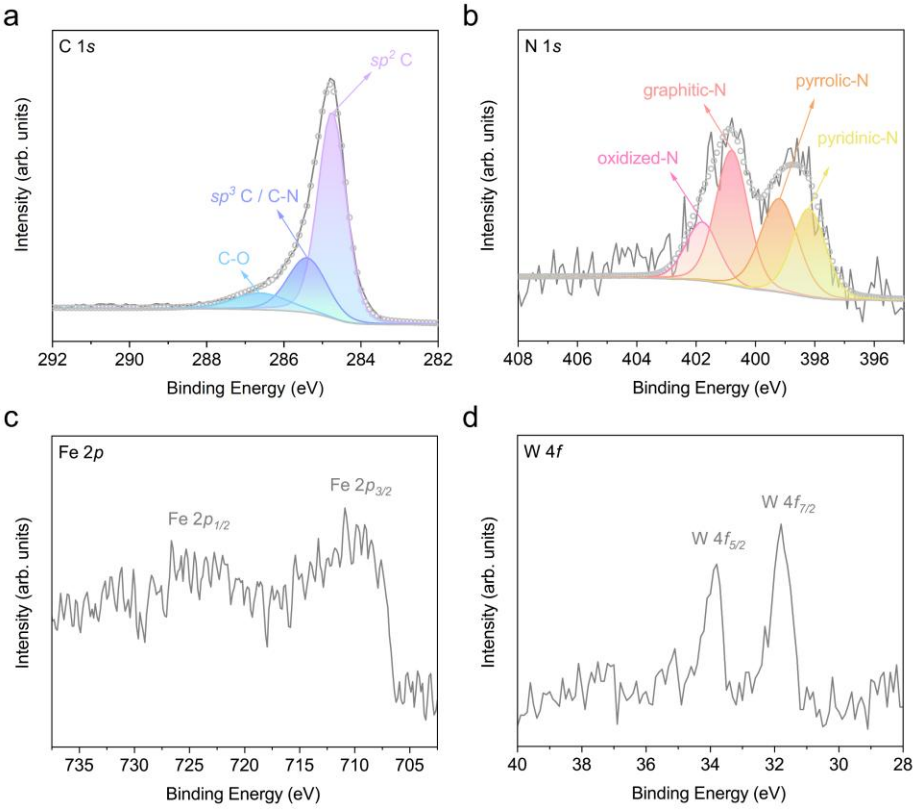

Supplementary Fig. 11. XPS analysis of Fe,W-N-C catalyst. **a**, High-resolution XPS spectrum of C 1*s*. **b**, High-resolution XPS spectrum of N 1*s*. **c**, High-resolution XPS spectrum of Fe 2*p*. **d**, High-resolution XPS spectrum of W 4*f*.

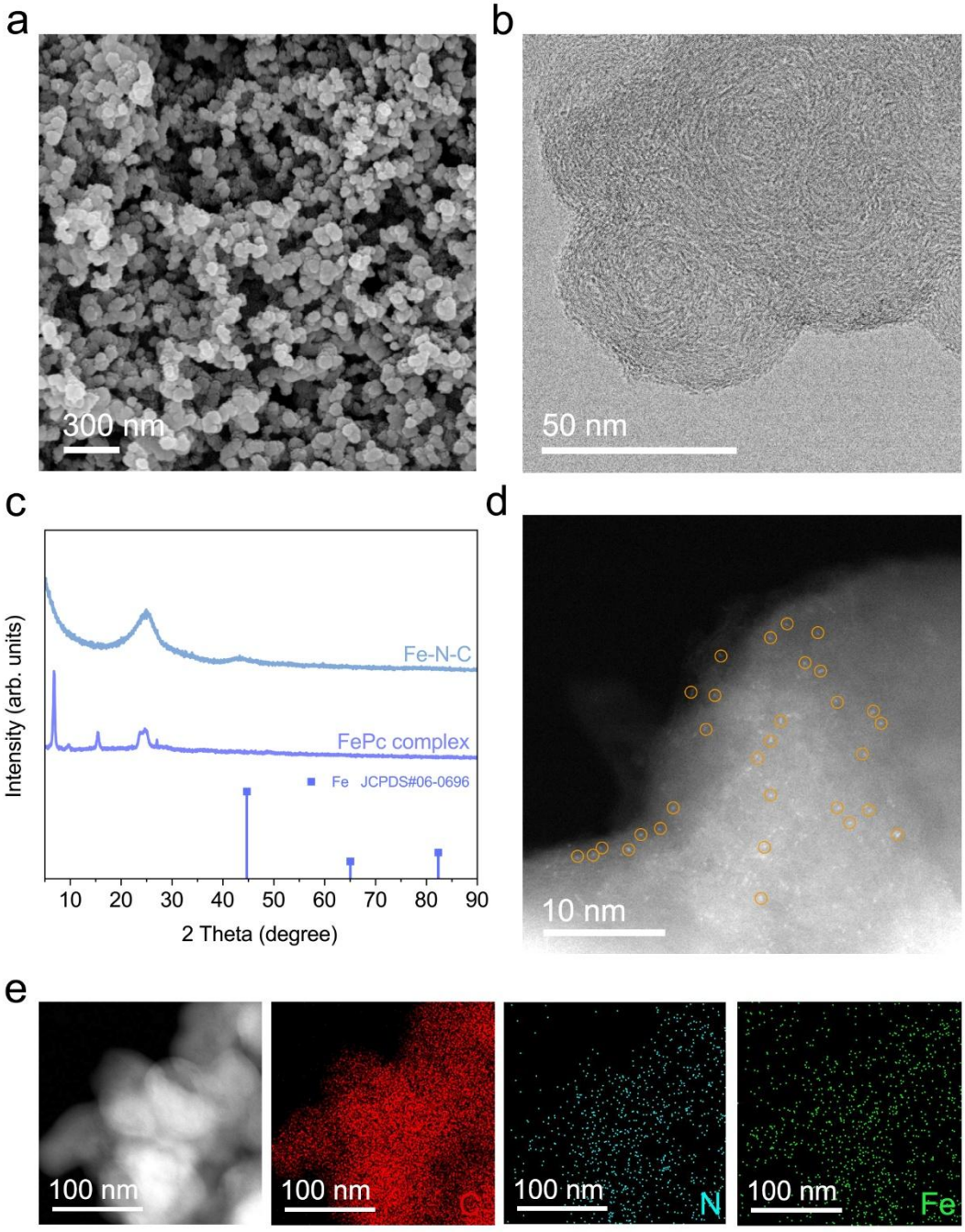

Supplementary Fig. 12. Morphological characterizations of Fe-N-C catalyst. **a**, SEM image. **b**, TEM image. **c**, XRD patterns of Fe-N-C catalyst and iron (II) phthalocyanine complex (FePc complex). **d**, Aberration-corrected HAADF-STEM image. **e**, HAADF-STEM image and corresponding EDX mapping images for C (red), N (blue) and Fe (green).

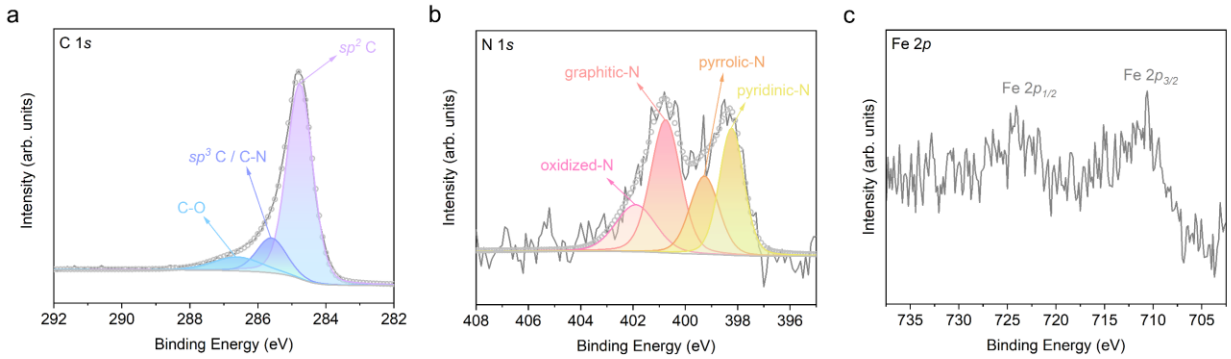

Supplementary Fig. 13. XPS analysis of Fe-N-C catalyst. **a**, High-resolution XPS spectrum of C 1*s*. **b**, High-resolution XPS spectrum of N 1*s*. **c**, High-resolution XPS spectrum of Fe 2*p*.

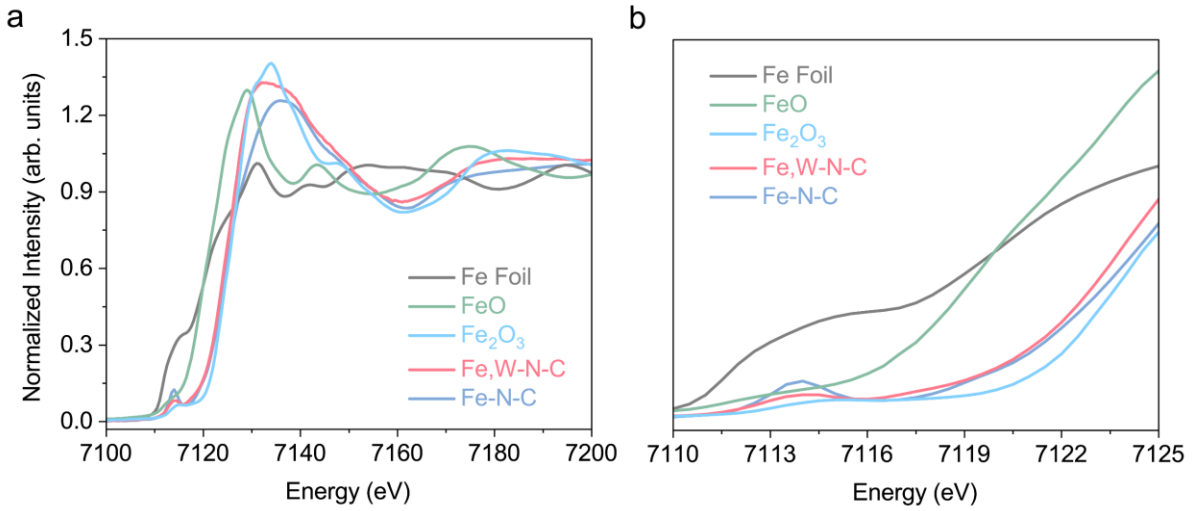

Supplementary Fig. 14. **a**, Normalized Fe K-edge X-ray absorption near-edge structure (XANES) spectra of Fe foil, FeO, Fe_2O_3, Fe,W-N-C and Fe-N-C. **b**, Expanded pre-edge region of Fe K-edge XANES spectra.

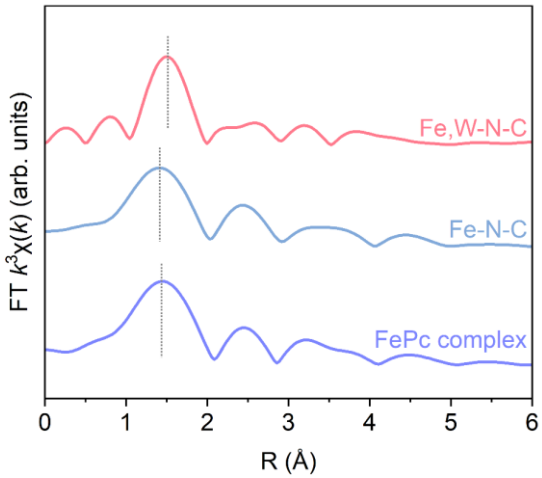

Supplementary Fig. 15. Fourier transformed extended X-ray absorption fine structure (FT-EXAFS) spectra at R space of FePc complex, Fe-N-C catalyst, and Fe,W-N-C catalyst.

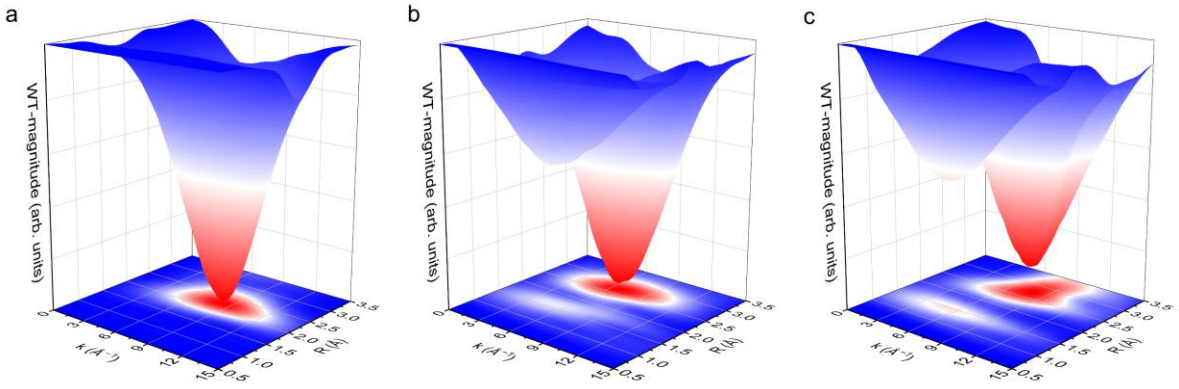

Supplementary Fig. 16. 3D contour wavelet transformed extended X-ray absorption fine structure maps of Fe foil (**a**), FeO (**b**) and Fe_2O_3 (**c**).

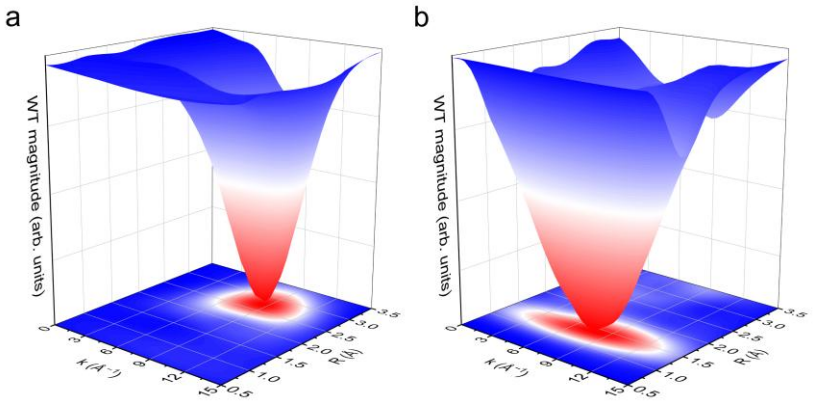

Supplementary Fig. 17. 3D contour wavelet transformed EXAFS maps of W powder (**a**) and WO_3 (**b**).

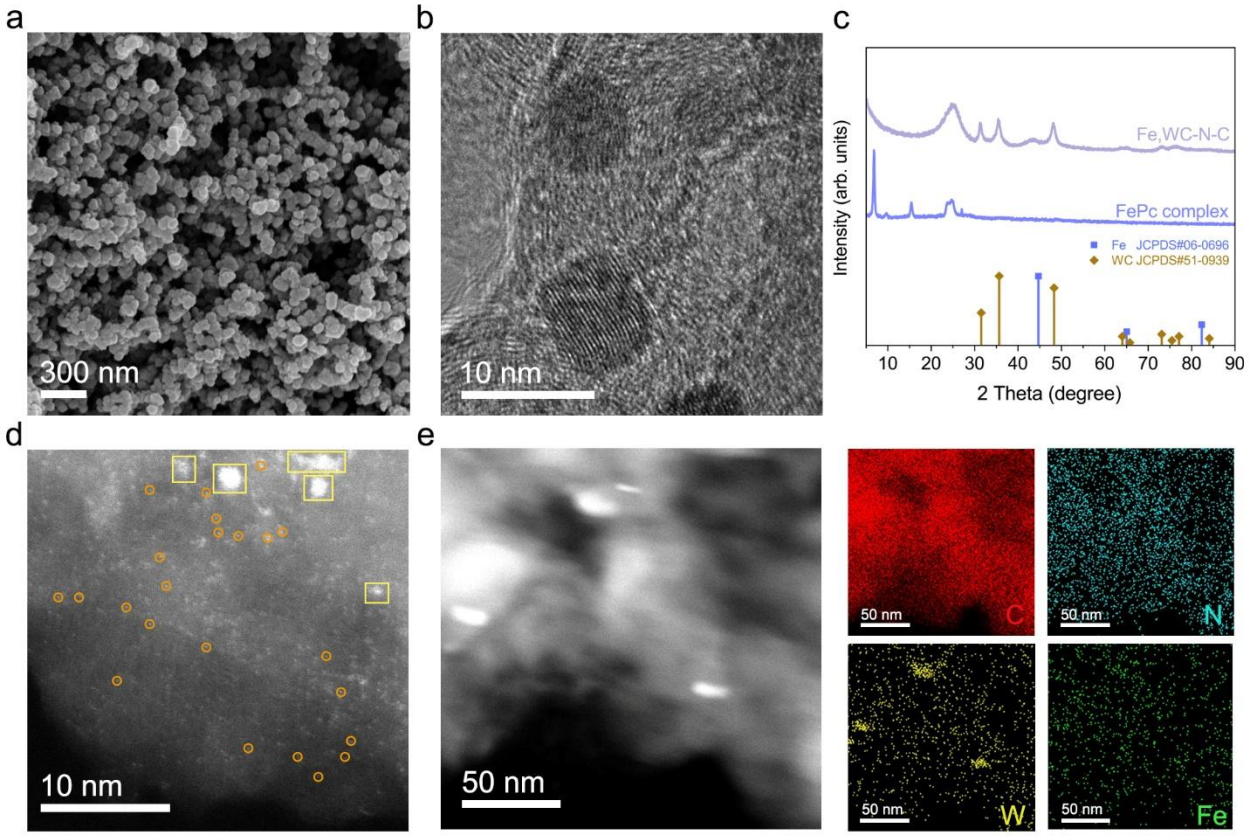

Supplementary Fig. 18. Morphological characterizations of Fe,WC-N-C catalyst. **a**, SEM image. **b**, TEM image. **c**, XRD patterns of Fe,WC-N-C catalyst and FePc complex. **d**, Aberration-corrected HAADF-STEM image. **e**, HAADF-STEM image and corresponding EDX mapping images for C (red), N (blue), W (yellow) and Fe (green).

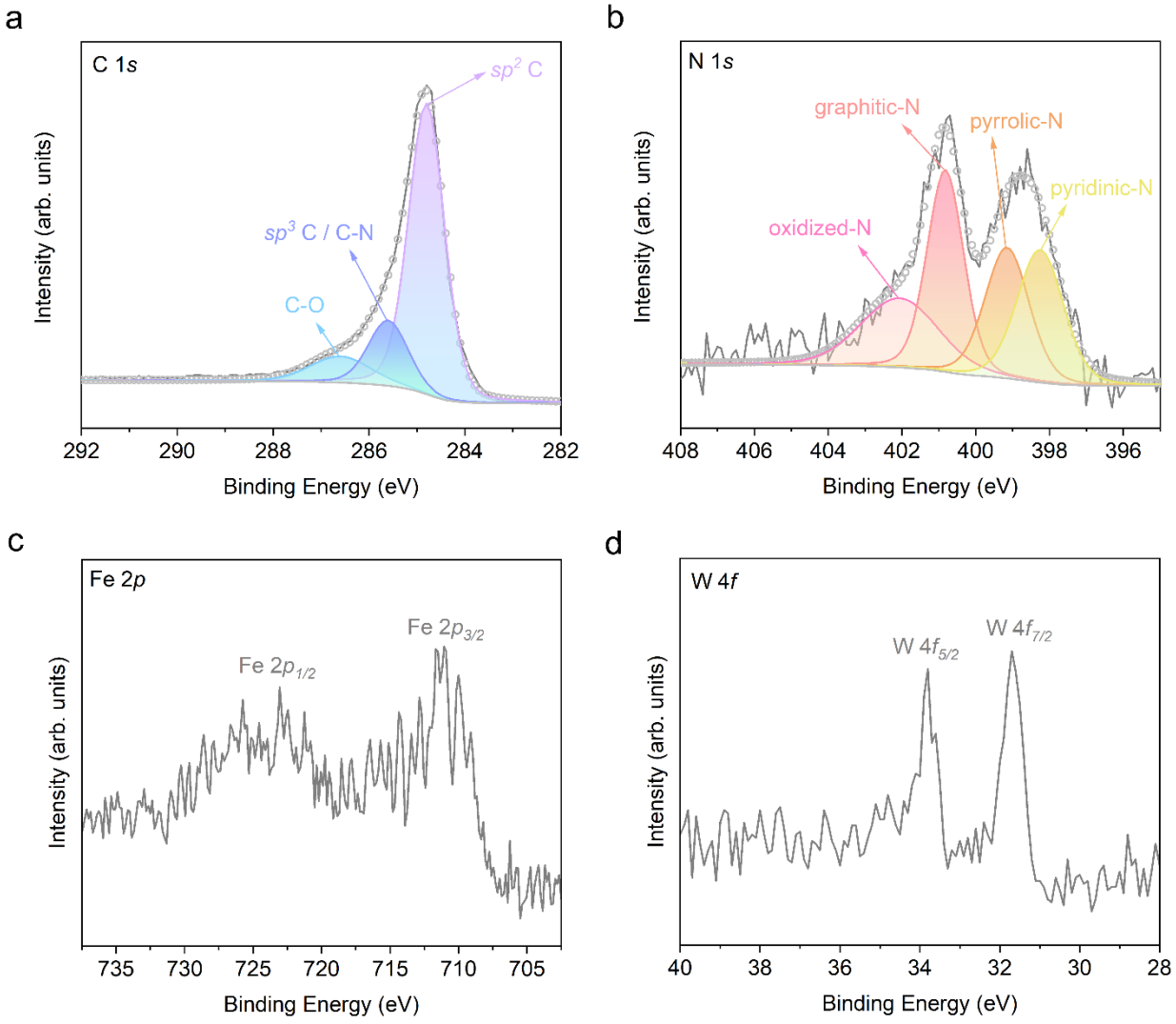

Supplementary Fig. 19. XPS analysis of Fe,WC-N-C. **a**, High-resolution XPS spectrum of C 1*s*. **b**, High-resolution XPS spectrum of N 1*s*. **c**, High-resolution XPS spectrum of Fe 2*p*. **d**, High-resolution XPS spectrum of W 4*f*.

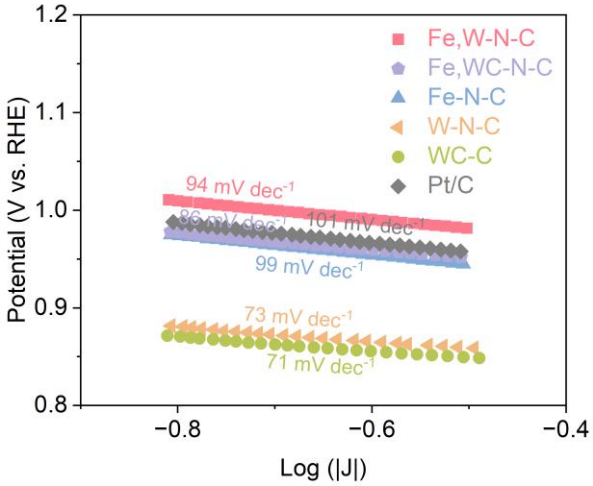

Supplementary Fig. 20. Tafel slopes for oxygen reduction reaction (ORR) of Fe,W-N-C, Fe,WC-N-C, Fe-N-C, W-N-C, WC-C and commercial 20 wt% Pt/C catalysts.

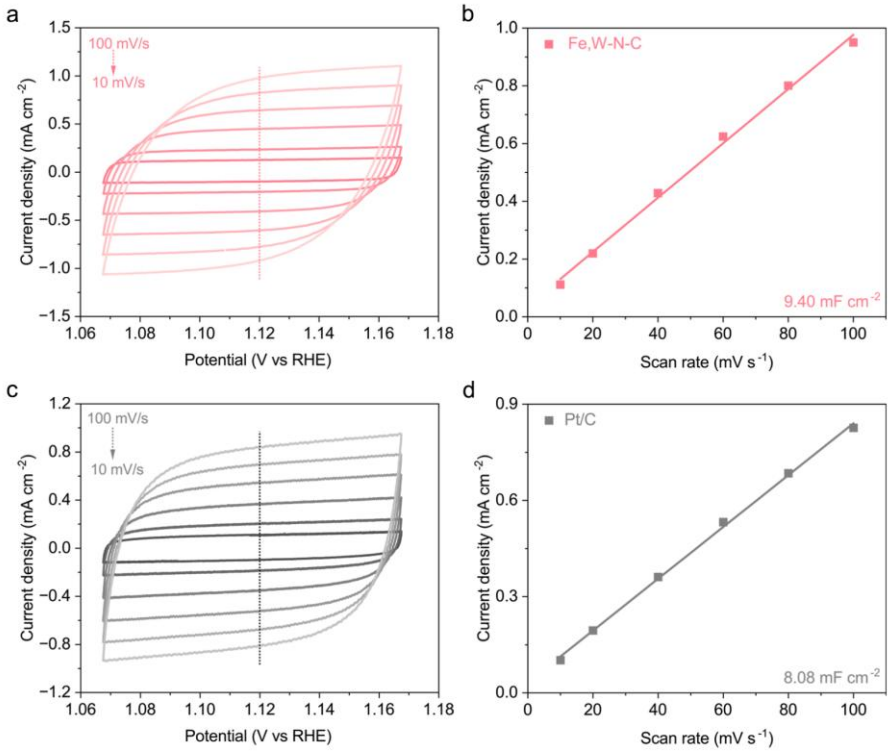

Supplementary Fig. 21. Cyclic voltammetry (CV) curves at different scan rates ranging from 10 to 100 mV s^{-1} of Fe,W-N-C (**a**) and Pt/C (**c**) catalysts. The capacitive current densities versus scan rates at 1.12 V versus RHE of Fe,W-N-C (**b**) and Pt/C (**d**) catalysts.

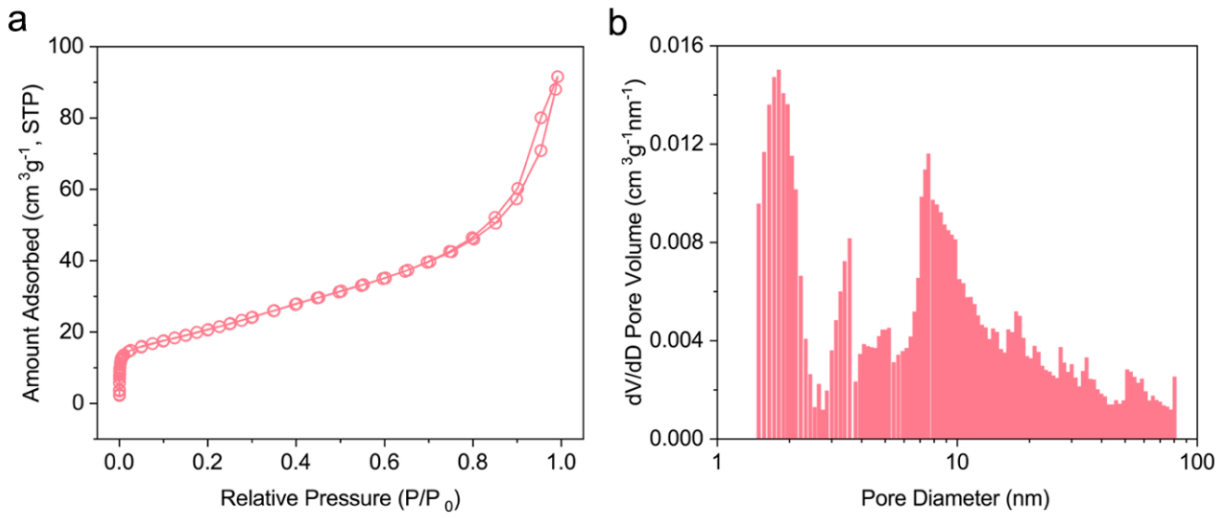

Supplementary Fig. 22. a, N_2 adsorption-desorption isotherms of Fe,W-N-C catalyst. **b**, The pore size distribution.

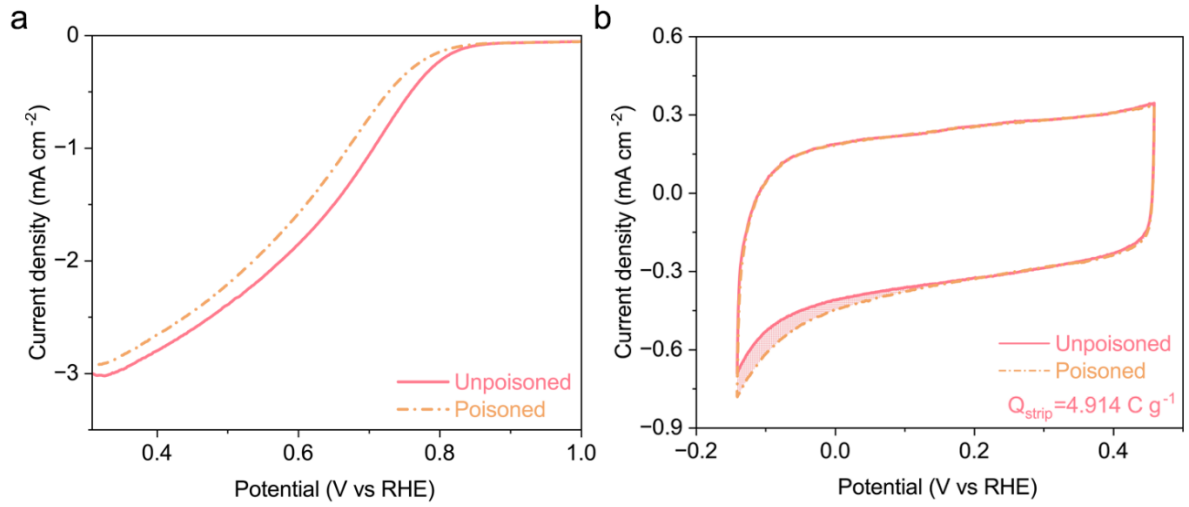

Supplementary Fig. 23. a, ORR performance of Fe,W-N-C catalyst before (unpoisoned) and during (poisoned) the nitrite adsorption. **b**, CV curves of the catalyst at unpoisoned and poisoned stages of the nitrite stripping protocol.

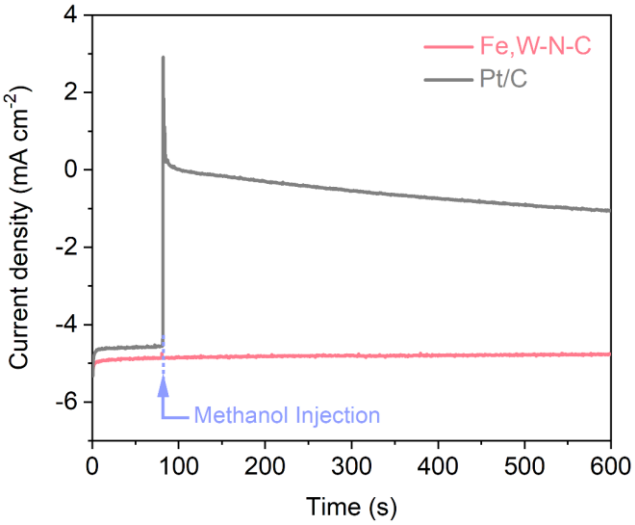

Supplementary Fig. 24. Methanol tolerance tests of Fe,W-N-C and commercial Pt/C catalysts at 0.70 V (V versus RHE). The chronoamperometric responses of the two catalysts before and after adding CH_3OH to the electrolyte.

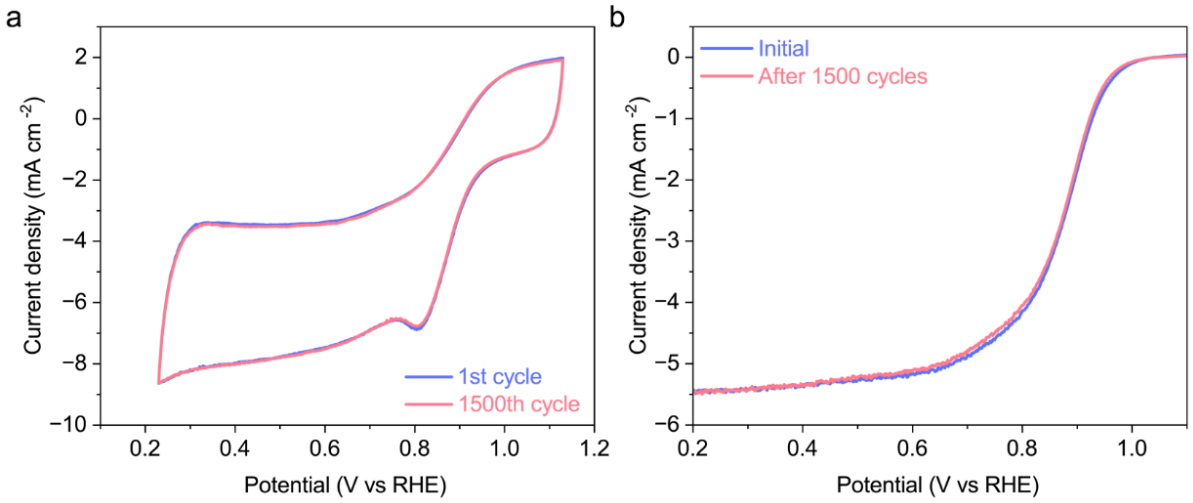

Supplementary Fig. 25. **a**, CV curves of the Fe,W-N-C catalyst at the 1st cycle and 1500th cycle in an O_2-saturated 0.1 M KOH electrolyte. **b**, ORR polarization curves for Fe,W-N-C catalyst before and after accelerated durability testing.

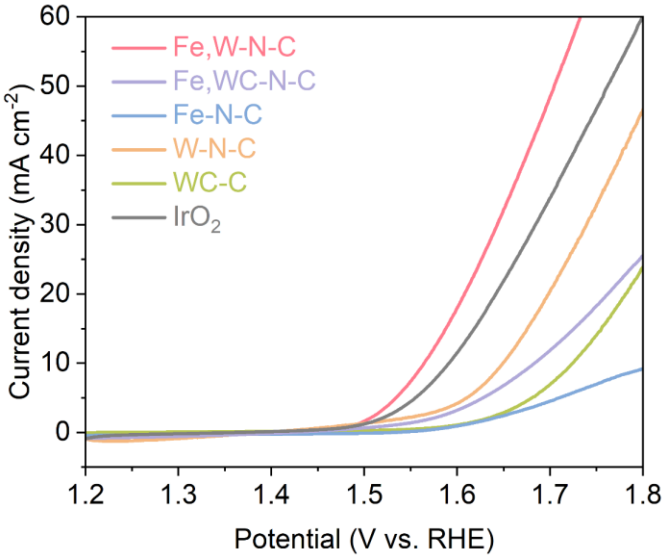

Supplementary Fig. 26. Oxygen evolution reaction (OER) polarization curves of Fe,W-N-C, Fe,WC-N-C, Fe-N-C, W-N-C, WC-C and commercial IrO_2 catalysts in 1.0 M KOH solution.

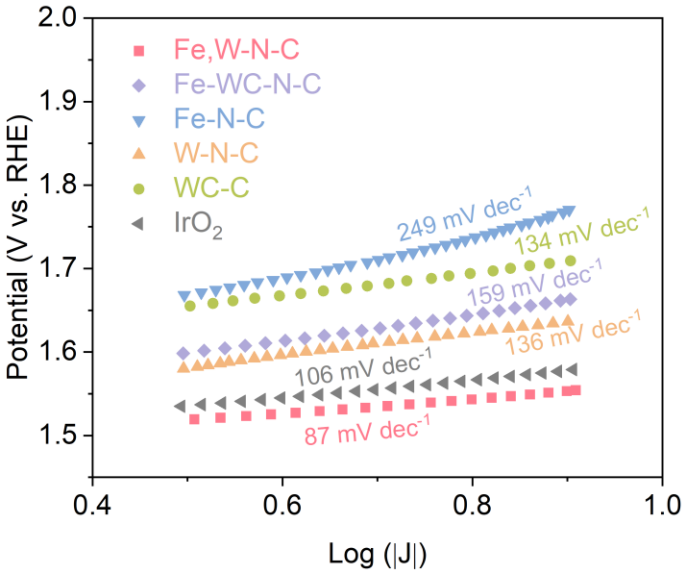

Supplementary Fig. 27. OER Tafel slopes of Fe,W-N-C, Fe,WC-N-C, Fe-N-C, W-N-C, WC-C and commercial IrO_2 catalysts.

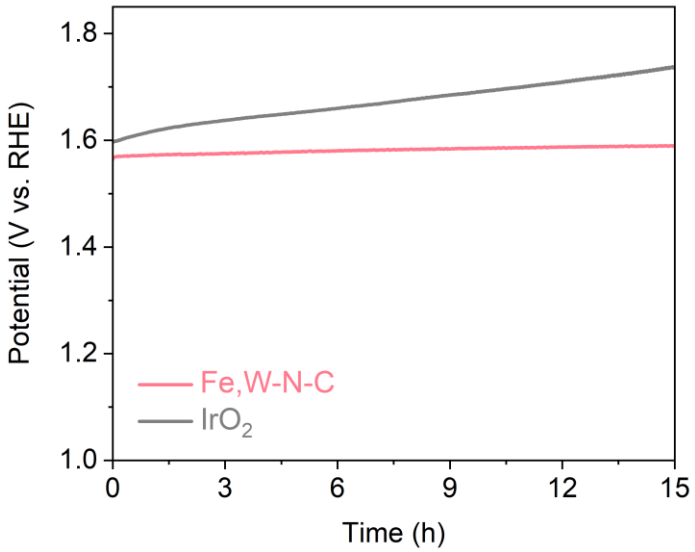

Supplementary Fig. 28. Long-term electrochemical OER stability tests of Fe,W-N-C and commercial IrO_2 catalysts.

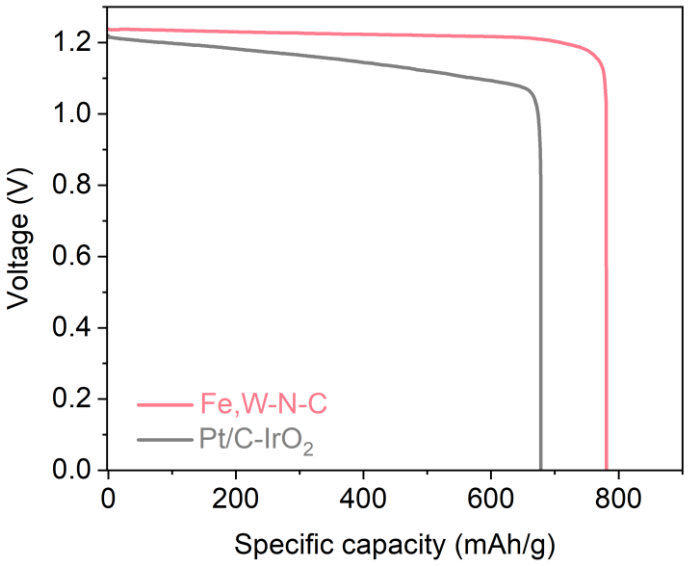

Supplementary Fig. 29. Specific capacity of zinc-air batteries (ZABs) with Fe,W-N-C catalyst and commercial Pt/C-IrO_2 catalyst as the air cathode.

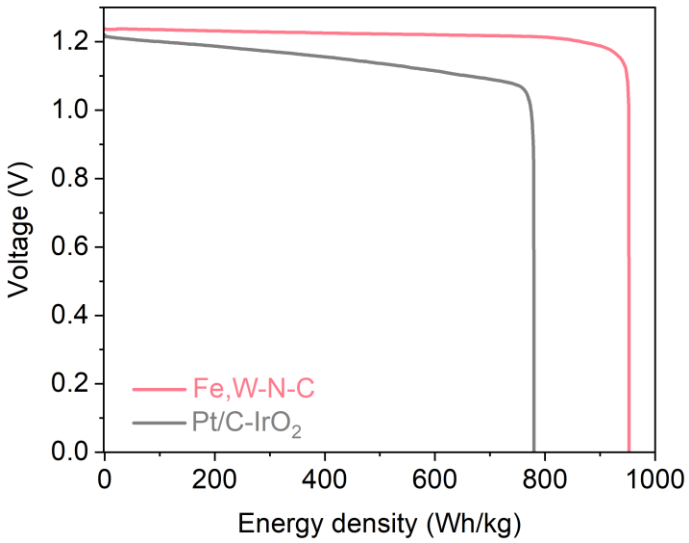

Supplementary Fig. 30. Energy density plots of ZABs with Fe,W-N-C catalyst and commercial Pt/C-IrO_2 catalyst as the air cathode.

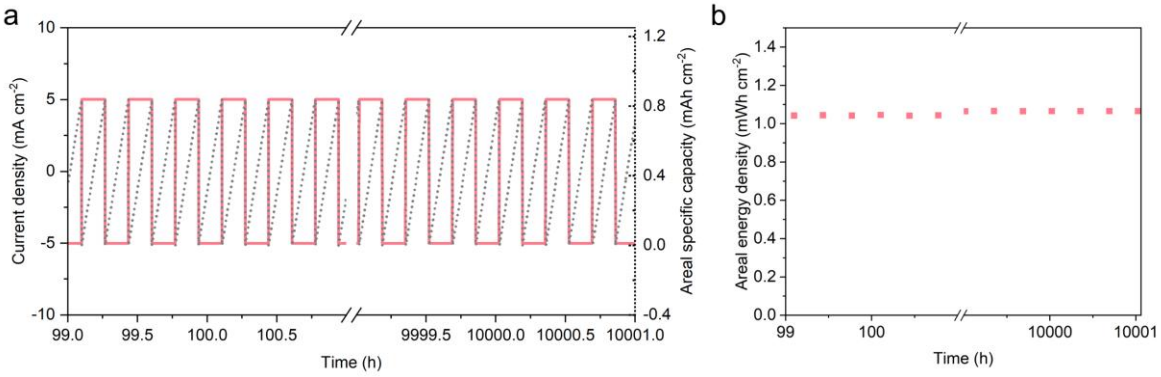

Supplementary Fig. 31. **a**, Enlarged current density and areal specific capacity profiles corresponds to Fig.5a. **b**, Areal energy density (based on the area of cathode) of Fe,W-N-C based ZAB at 99-101 hours and 9999-10001 hours during discharge/charge cycling at the current density of 5 mA cm^{-2}.

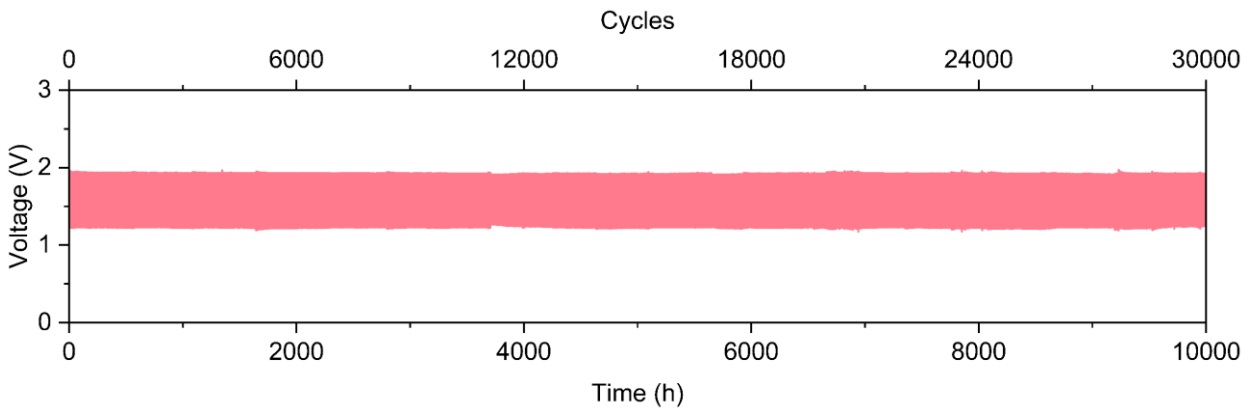

Supplementary Fig. 32. Repeated galvanostatic discharge/charge cycling stability test for liquid-state ZAB with Fe,W-N-C air cathode at a current density of 5 mA cm^{-2}.

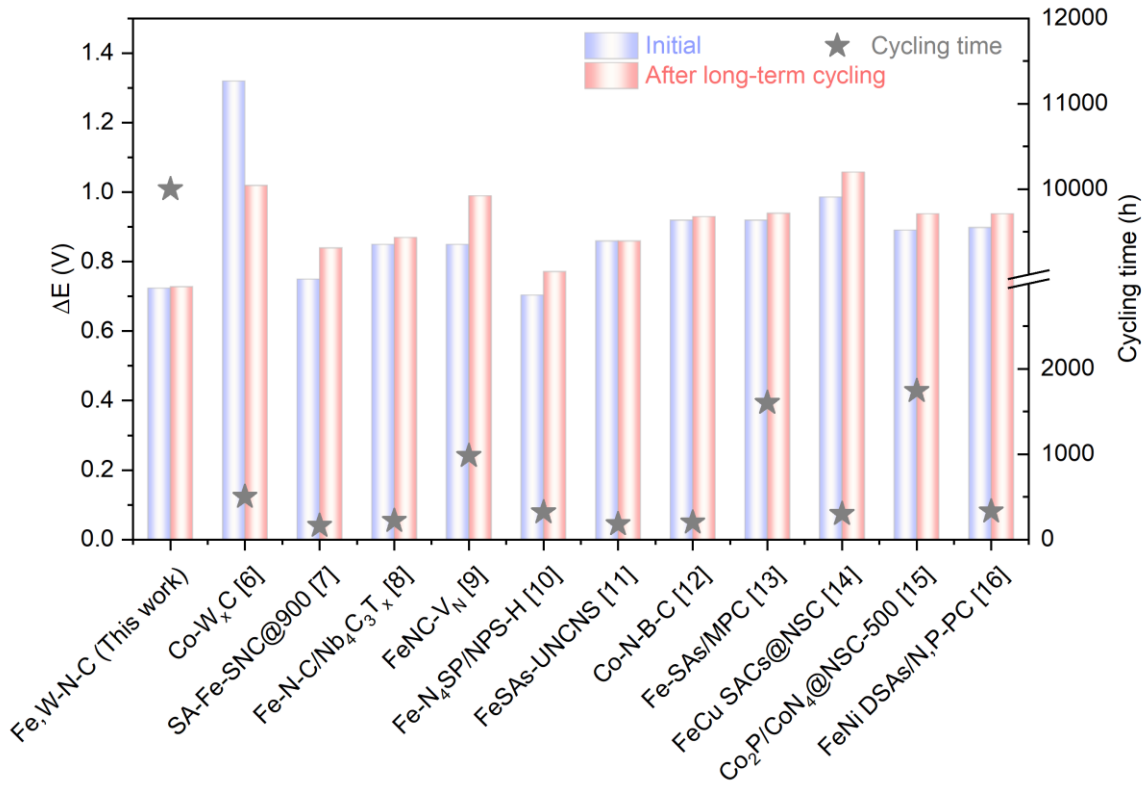

Supplementary Fig. 33. The ZABs performance (charge and discharge potential difference in initial and after long term cycling, and cycling time) comparison at the current density of 5 mA cm^{-2} for Fe,W-N-C with other state-of-the-art catalysts[6-16].

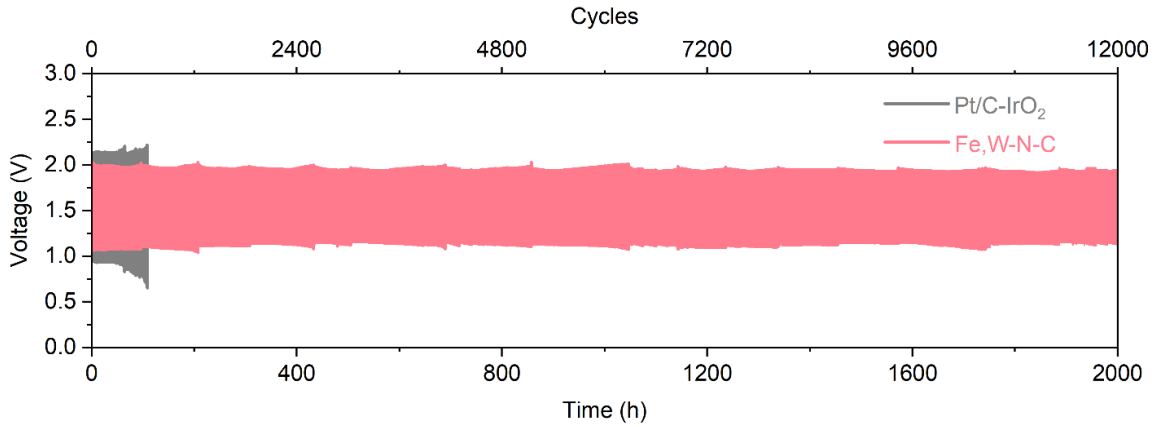

Supplementary Fig. 34. Galvanostatic discharge/charge cycling stabilities for liquid-state ZABs with Fe,W-N-C and Pt/C-IrO_2 air cathodes at a current density of 50 mA cm^{-2}.

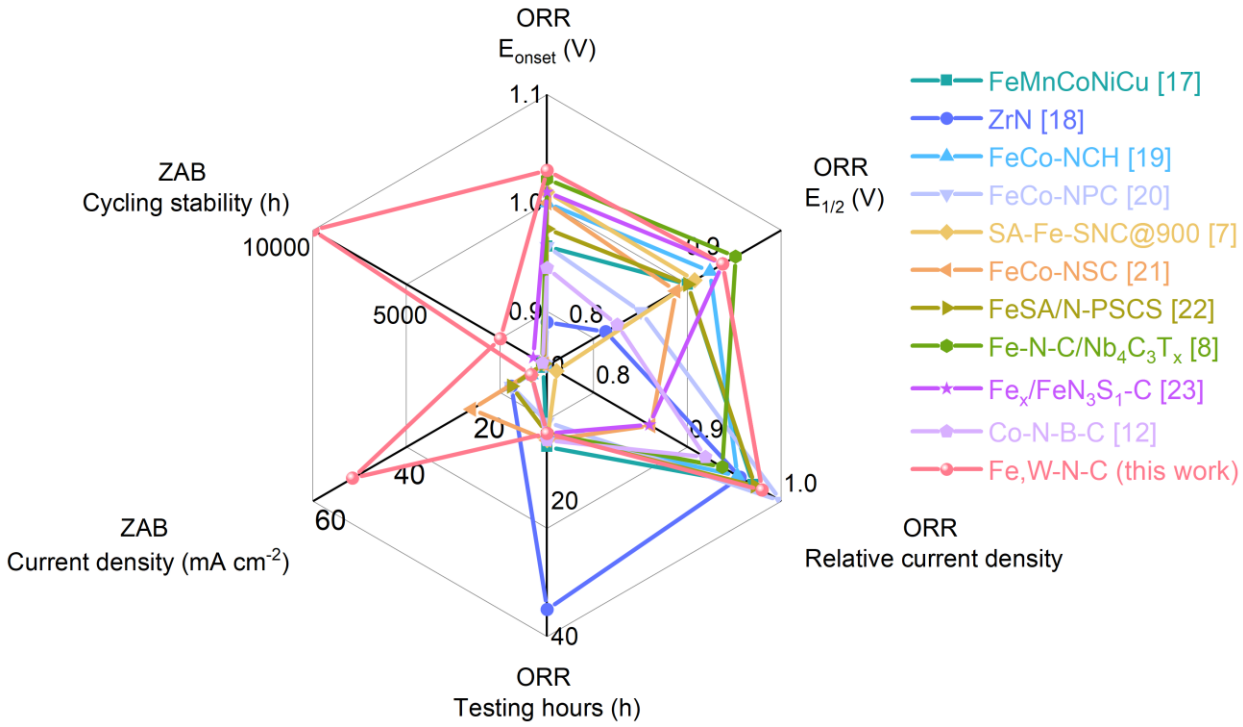

Supplementary Fig. 35. Comparison of ORR electrocatalytic performance and ZABs cycling lifetime of Fe,W-N-C catalyst with some previously reported catalysts[7,8,12,17-23].

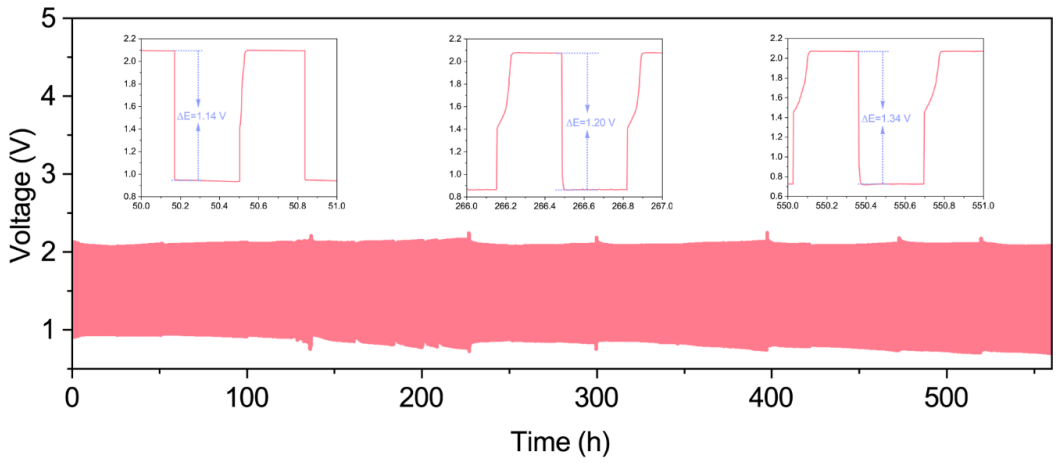

Supplementary Fig. 36. Galvanostatic discharge/charge cycling stability test for liquid-state ZAB based on Fe,W-N-C air cathode at the current density of 100 mA cm^{-2}.

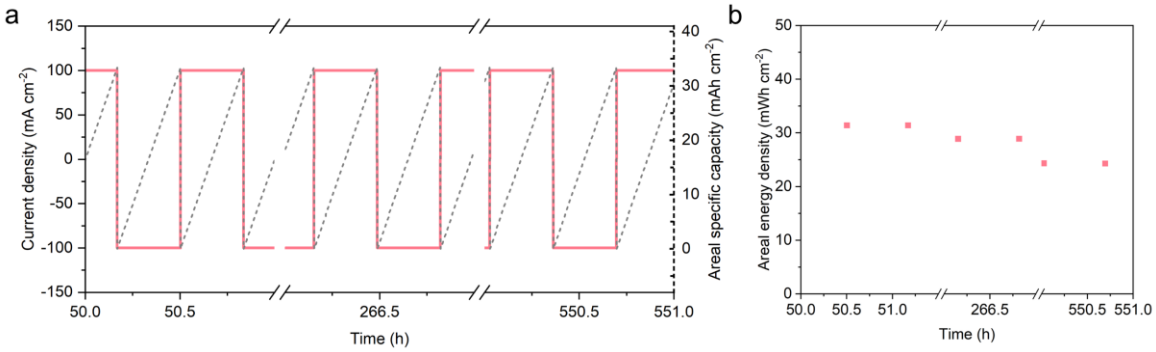

Supplementary Fig. 37. a, Enlarged current density and areal specific capacity profiles corresponds to Supplementary Fig. 36. **b**, Areal energy densities (based on the area of cathode) of Fe,W-N-C based ZAB at 50-52 hours, 266-267 hours, and 550-551 hours during discharge/charge cycling at the current density of 100 mA cm^{-2}.

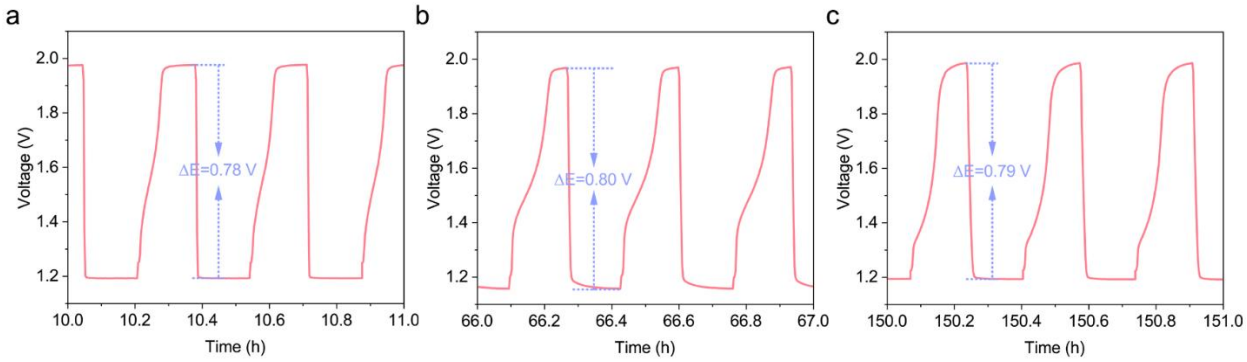

Supplementary Fig. 38. The enlarged voltage profile of the flexible solid-state ZAB with Fe,W-N-C catalyst as the air cathode at the flat (**a**) / bent (**b**) / revert flat (**c**) states.

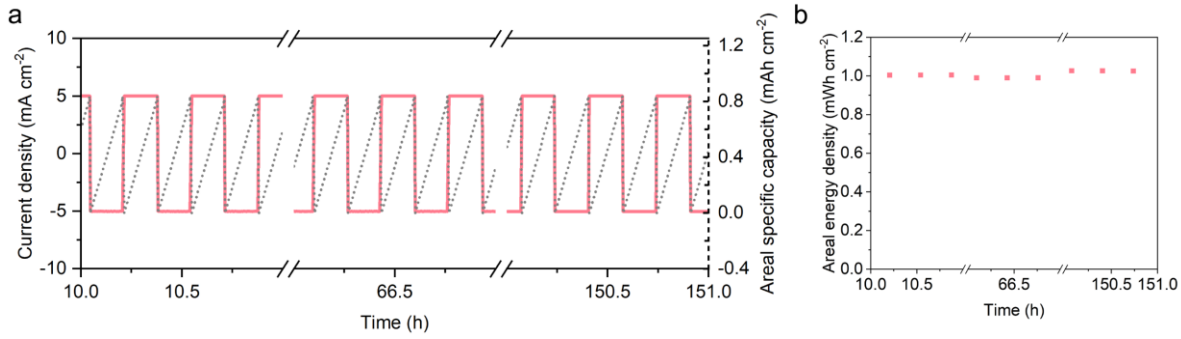

Supplementary Fig. 39. a, Enlarged current density and areal specific capacity profiles corresponds to Fig. 5c and Supplementary Fig. 38. **b**, Areal energy densities (based on the area of cathode) of Fe,W-N-C based ZAB at flat state (10-11 hours), bent state (66-67 hours), and revert flat state (150-151 hours) during discharge/charge cycling at the current density of 5 mA cm^{-2}.

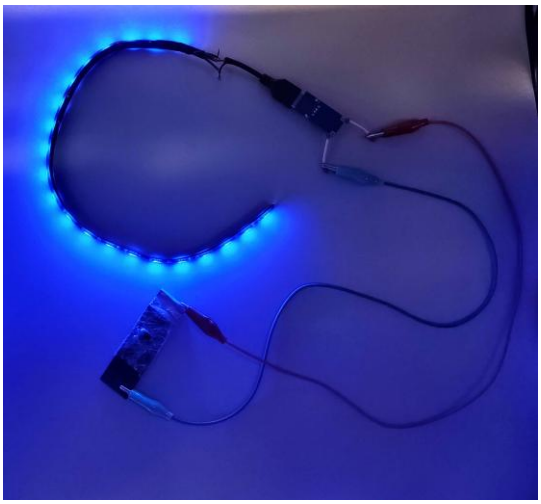

Supplementary Fig. 40. Photograph of a wristband with LED lights powered by the flexible solid-state ZAB with Fe,W-N-C catalyst as the air cathode.

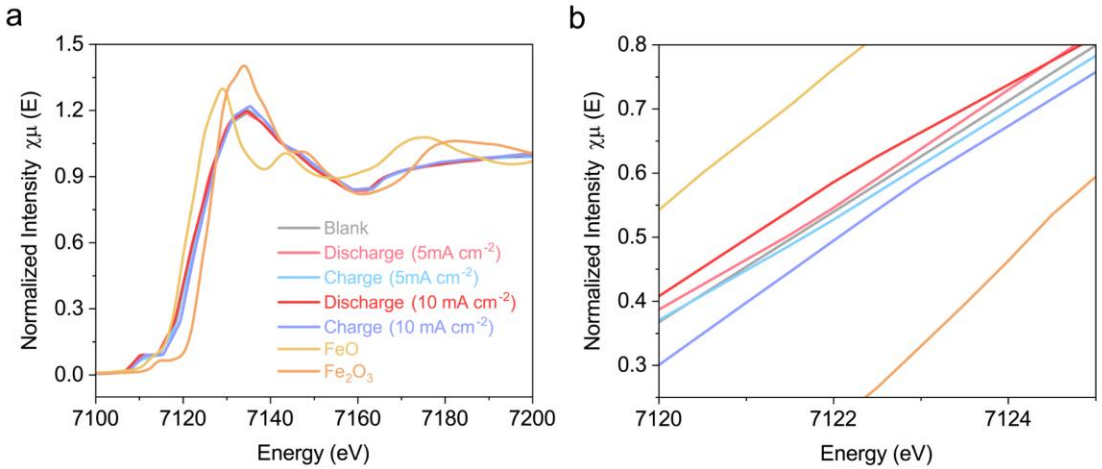

Supplementary Fig. 41. In situ XAS characterizations. **a**, Fe K-edge XANES spectra of Fe,W-N-C based ZAB during charge and discharge processes at different current densities. **b**, Enlarged view of the adsorption edge of XANES spectra.

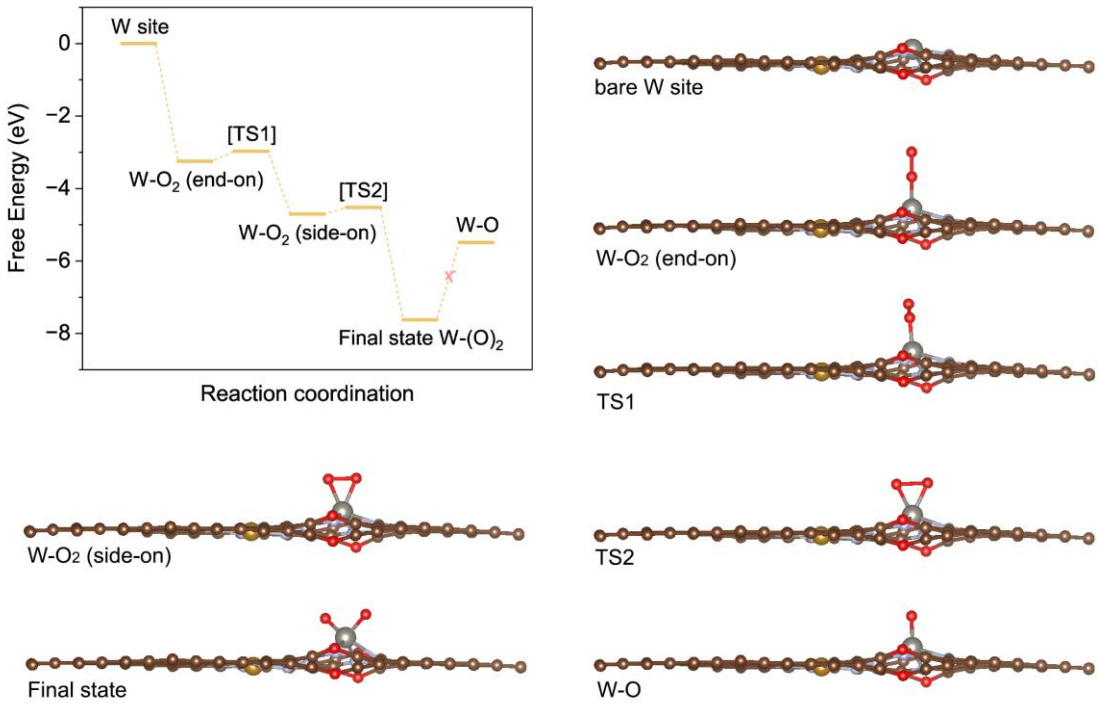

Supplementary Fig. 42. The atomistic structure and free energy of the initial, transition, and final states of the adsorption and dissociation reactions of O_2 on the W-N_4 site in Fe,W-N-C catalyst.

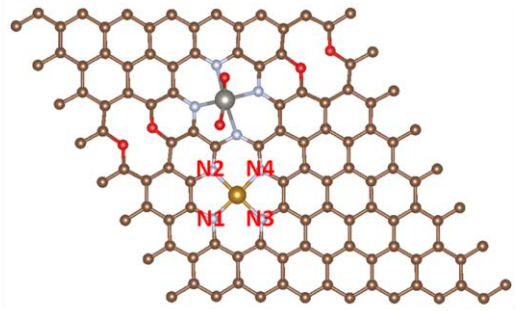

Sites	Charge for N and Fe in Fe-N-C	Charge for N and Fe in Fe,W-N-C
N1	-1.158	-1.247
N2	-1.176	-1.181
N3	-1.176	-1.067
N4	-1.097	-1.151
Fe	+1.085	+1.103

Supplementary Fig. 43. The Bader charge analysis of Fe and N atoms in Fe-N_4 site and Fe-N_4/W-N_4O_2 site.

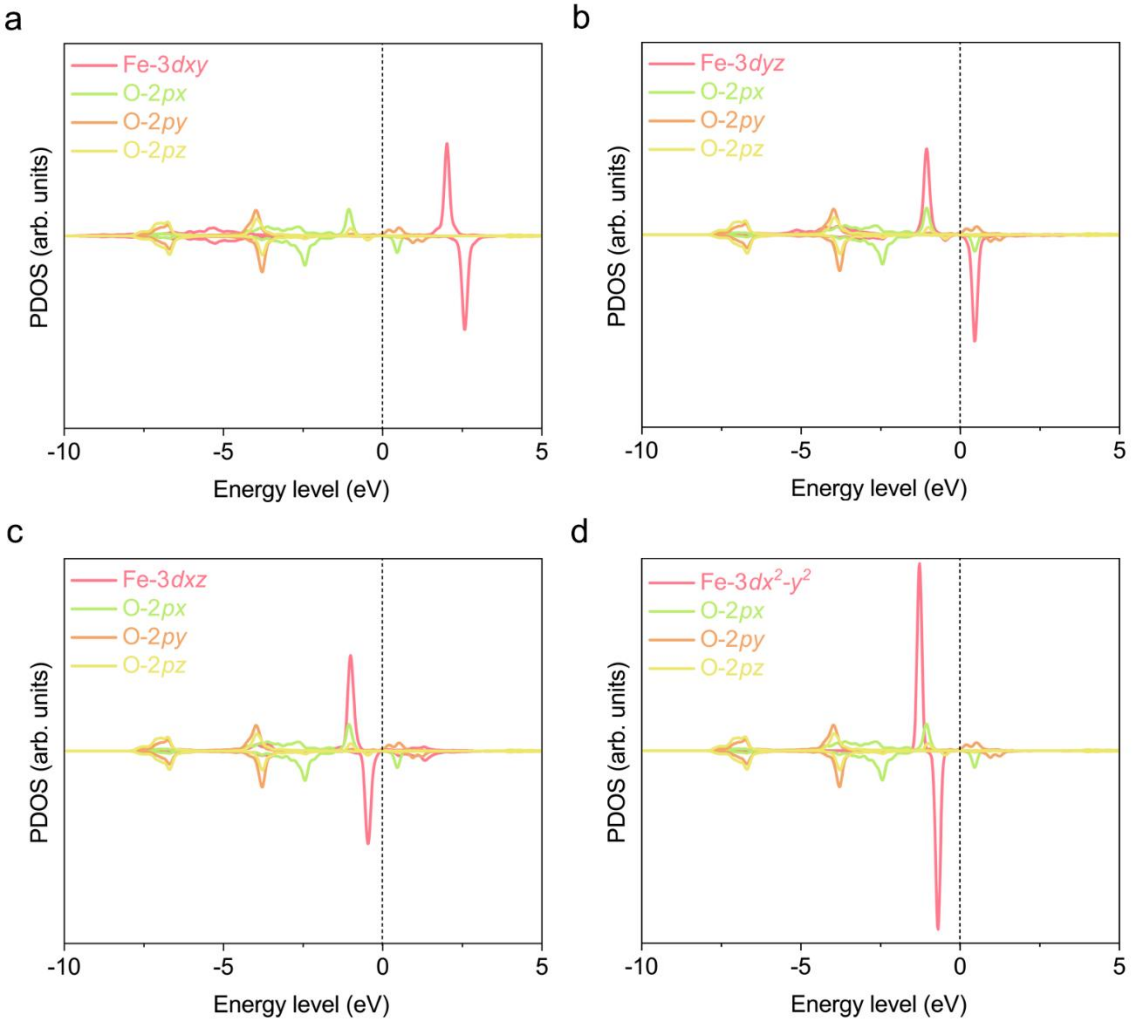

Supplementary Fig. 44. Projected density of state analysis of (**a**) Fe-3*dxy*, (**b**) Fe-3*dyz*, (**c**) Fe-3*dxz* and (**d**) Fe-3dx^2-y^2 orbitals with O 2*px*/2*py*/2*pz* orbitals in *OH intermediate on Fe-N_4/W-N_4 site.

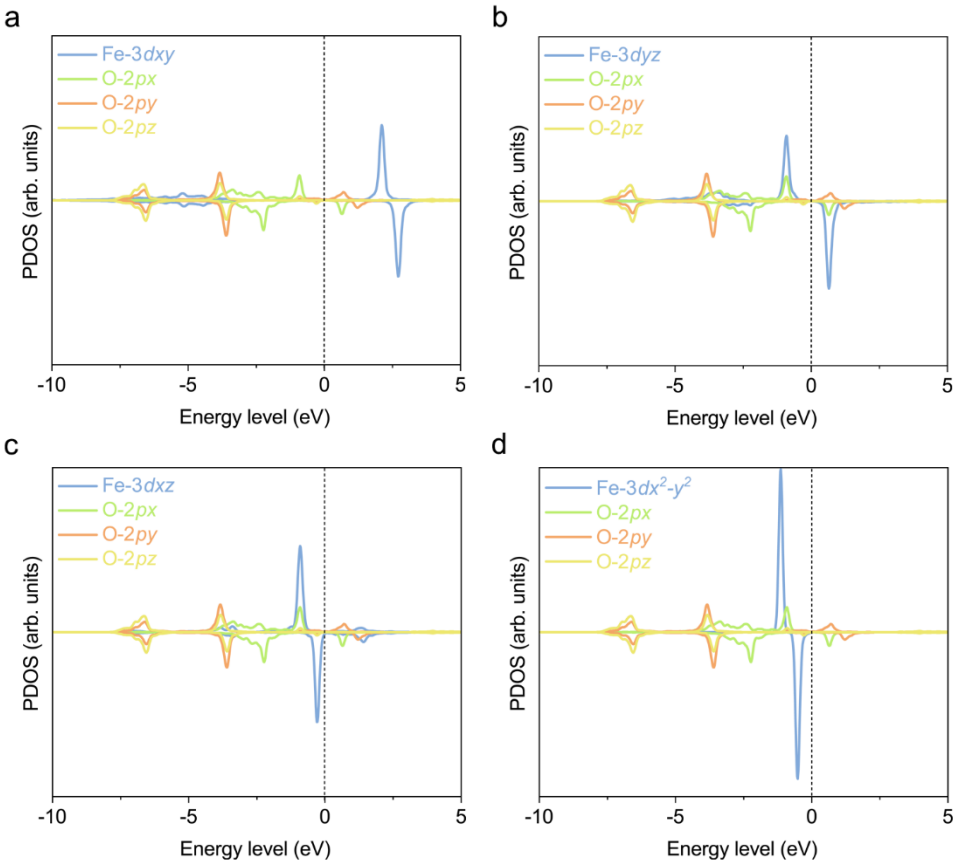

Supplementary Fig. 45. Projected density of state analysis of (**a**) Fe-3*dxy*, (**b**) Fe-3*dyz*, (**c**) Fe-3*dxz* and (**d**) Fe-3dx^2-y^2 orbitals with O 2*px*/2*py*/2*pz* orbitals in *OH intermediate on Fe-N_4 site.

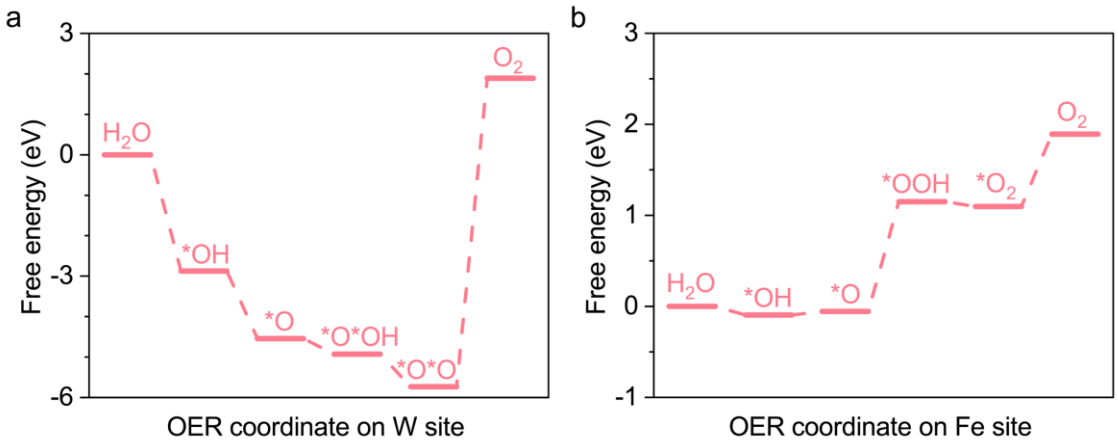

Supplementary Fig. 46. The free energy diagram of OER through a $4e^-$ pathway on the W-N_4 site (**a**) and Fe-N_4 site (**b**) in Fe,W-N-C catalyst.

Supplementary Tables

Supplementary Table 1. Inductively coupled plasma-optical emission spectroscopy (ICP-OES) analysis results of the as-prepared catalysts.

Catalyst	M (M=Fe/Co/Ni, wt%)	W (wt%)
Fe,W-N-C	1.25	4.02
Fe,WC-N-C	1.56	5.49
Fe-N-C	1.34	N/A
W-N-C	N/A	4.76
WC-N-C	N/A	6.23
Co,W-N-C	1.18	4.06
Ni,W-N-C	1.30	4.04

Supplementary Table 2. Extended X-ray absorption fine structure (EXAFS) fitting parameters for Fe foil, WO_3 and Fe,W-N-C catalyst.

Sample	Bond Type	Coordination Number	Bond Length R (Å)	Bond disorder σ^2 (Å^2)	*R* factor
Fe foil	Fe-Fe	8	2.47±0.02	0.0049	0.0023
	Fe-Fe	6	2.85±0.01	0.0062	
Fe,W-N-C	Fe-N	4	1.90±0.06	0.0027	0.0107
	Fe-C	4	2.69±0.08	0.0057	
	Fe-C	4	3.01±0.09	0.0025	
	Fe-N (bond with W)	1	3.33±0.04	0.0023	
WO_3	W-O	4	1.80±0.01	0.0054	0.0072
	W-O	2	2.15±0.03	0.0052	
Fe,W-N-C	W-N	4	2.08±0.09	0.0014	0.0164
	W-C	4	2.88±0.04	0.0025	
	W-C	4	3.21±0.06	0.0054	
	W-C	4	3.65±0.06	0.0007	
	W-N (bond with Fe)	1	4.29±0.05	0.0055	

Supplementary Table 3. Summary of the onset potential (E_{onset}), half-wave potential ($E_{1/2}$), and J_k at 0.82 V of different catalysts.

Sample	E_{onset} Potential (V, V versus RHE)	$E_{1/2}$ Potential (V, V versus RHE)	J_k (mA cm^{-2})
Fe,W-N-C	1.03 ± 0.018	0.90 ± 0.010	17.14
Fe,WC-N-C	1.00 ± 0.022	0.87 ± 0.005	13.96
Fe-N-C	0.99 ± 0.011	0.84 ± 0.012	7.26
W-N-C	0.90 ± 0.009	0.79 ± 0.020	1.59
WC-N-C	0.88 ± 0.010	0.77 ± 0.013	1.10
Pt/C	1.01 ± 0.013	0.85 ± 0.017	9.64

Supplementary Table 4. Summary of Tafel slopes for ORR of the as-prepared catalysts.

	Fe,W-N-C	Fe,WC-N-C	Fe-N-C	W-N-C	WC-N-C	Pt/C
Tafel Slope (mV/dec)	94	86	99	73	71	101

Supplementary Table 5. ORR electrocatalytic performance comparison of Fe,W-N-C with other state-of-the-art catalysts in 0.1 M KOH.

Catalyst	Loading Amount (mg cm^{-2})	E_{onset}	$E_{1/2}$	Stability	Ref.
Fe,W-N-C	**0.2**	**1.03**	**0.90**	**97.94% after 36000 s**	**This Work**
$Co(CN)_3$-Cub	2.04	0.99	0.90	$E_{1/2}$ −20 mV after 10000 cycles	[24] *Nat. Catal.* **6**, 1164-1173 (2023)
HESA	0.127	0.96	0.87	97% after 43200 s	[17] *Nat. Sustain*. **6**, 816-826 (2023)
(101) copper phosphosulfide	0.1	-	0.90	$E_{1/2}$ −11 mV after 30000 cycles	[25] *Nat. Energy* **6**, 592-604 (2021)
ZrN NPs	0.125	0.89	0.80	95.6% after 36 h	[18] *Nat. Mater.* **19**, 282-286 (2020)
4.3% NiFe-MOF	2.0	0.92	0.83	97% after 200 h	[26] *Nat. Energy* **4**, 115-122 (2019)
NFLGDY-900c	0.6	-	0.87	92% after 10000 s	[27] *Nat. Chem.* **10**, 924-931 (2018)
FeCo-NCH	0.33	-	0.889	$E_{1/2}$ −8 mV after 10000 cycles	[19] *Nat. Commun.* **14**, 1822 (2023)
HESACs (FeCoNiCuMn)	0.18	0.999	0.887	93.33% after 25000 s	[28] *Nat. Commun.* **13**, 5071 (2022)
Co SA-NDGs	0.3	1.02	-	$E_{1/2}$ −11 mV after 5000 cycles	[29] *Nat. Commun.* **13**, 3689 (2022)
FeNC-V_N	0.3	0.99	0.902	No degradation after 5000 cycles	[8] *J. Am. Chem. Soc.* **146**, 4803-4813 (2024)
P/Fe-N-C	0.6	1.01	0.90	$E_{1/2}$ −2 mV after 36000 s	[30] *J. Am. Chem. Soc.* **145**, 3647-3655 (2023)
MNCSs	0.126	-	0.82	$E_{1/2}$ −6mV after 5000 cycles	[31] *J. Am. Chem. Soc.* **144**, 11767-11777 (2022)
Co-Fe ZIF (S-CFZ)	0.3	-	0.85	91% after 100 h	[32] *J. Am. Chem. Soc.* **144**, 4783-4791 (2022)
Fe-Co-Ni MOF	0.28	0.82	0.75	-	[33] *J. Am. Chem. Soc.* **144**, 3411-3428 (2022)
Ru-SAS/SNC	0.4	0.998	0.861	$E_{1/2}$ −24 mV after 30000 cycles	[34] *J. Am. Chem. Soc.* **144**, 2197-2207 (2022)
Mn-RuO_2	0.2	-	0.86	95.5% after 50 h	[35] *J. Am. Chem. Soc.* **144**, 2694-2704 (2022)

FeCo-NPC	0.51	0.96	0.83	no obvious change after 30000 s	[20] *Adv. Mater.* **36**, 2306047 (2024)
YN_4-Cl	0.41	0.93	0.85	95% after 43200 s	[36] *Adv. Mater.* **35**, 2300381 (2023)
Fe_H-N-C	0.6	-	0.91	$E_{1/2}$ −29 mV after 100000 cycles	[37] *Adv. Mater.* **35**, 2210714 (2023)
H-3DOM-Co/ONC	0.2	0.94	0.84	94% after 30000 s	[38] *Adv. Mater.* **35**, 2301894 (2023)
V-CMO/5rGO	0.255	-	0.86	90% after 36000 s	[39] *Adv. Mater.* **35**, 2303109 (2023)
DAF-COF	0.167	0.89	0.74	94.3% after 36000 s	[40] *Adv. Mater.* **35**, 2209129 (2023)
Fe-Zn@SNC	0.51	0.99	0.86	$E_{1/2}$ −25 mV after 2000 cycles	[41] *Angew. Chem. Int. Ed.* **135**, e202301833 (2023)
Pd-Gd_2O_3/C	0.255	0.986	0.877	90.1 % after 39600 s	[42] *Angew. Chem. Int. Ed.* **62**, e202314565 (2023)
Mn-SAS	-	0.99	0.85	98.5% after 22000 s	[43] *Angew. Chem. Int. Ed.* **62**, e202314933 (2023)
SA-Fe-SNC@900	0.255	1.01	0.876	94.4% after 40000 s	[7] *Adv. Mater.* **35**, 2209948 (2023)
Co-N-B-C	0.102	0.94	0.81	91.9% after 40000 s	[12] *Energy Environ. Mater.* **7**, e12569 (2024)
FeCo-NSC	0.4	-	0.86	86.1% after 40000 s	[21] *Energy Storage Mater.* **45**, 805-813 (2022)
FeSA/N-PSCS	0.4	0.976	0.87	$E_{1/2}$ −3 mV after 5000 cycles	[22] *Energy Storage Mater.* **59**, 102790 (2023)
Fe_x/FeN_3S_1-C	0.255	1.01	0.9	85.92% after 36000 s	[23] *Energy Environ. Sci.* **17**, 4746-4757 (2024)

Supplementary Table 6. Summary of the potential at a constant current density of 10 mA cm^{-2} ($E_{J=10}$) and Tafel slopes for OER of the as-prepared catalysts.

	Fe,W-N-C	Fe,WC-N-C	Fe-N-C	W-N-C	WC-N-C	IrO_2
$E_{J=10}$ (V)	1.56	1.68	1.81	1.64	1.72	1.59
Tafel Slope (mV/dec)	87	159	249	136	134	106

Supplementary Table 7. The zinc-air batteries performance comparison of Fe,W-N-C with other state-of-the-art catalysts.

Catalyst	Loading Amount (mg cm^{-2})	Cycling Stability (h/cycles)	Current Density (mA cm^{-2})	Ref.
Fe,W-N-C	**0.5**	**Over 10,000 h (30,000 cycles)**	**5**	**This work**
	1.0	**Over 2,000 h 12,000 cycles**	**50**	
	1.0	**Over 550 h 825 cycles**	**100**	
HESA (FeMnCoNiCu)	1.0	200 h	2	[17] *Nat. Sustain.* **6**, 816-826 (2023)
(101)-copper phosphosulfide	15.0	800 h	25	[25] *Nat. Energy* **6**, 592-604 (2021)
ZrN nanoparticles	1.0	100 h	10	[18] *Nat. Mater.* **19**, 282-286 (2020)
PdMo bimetallene/C	1.0	500 h	10	[44] *Nature* **574**, 81-85 (2019)
CuNa-CF	0.2	5000 h	1	[45] *Nat. Commun.* **15**, 8365 (2024)
FeCo-NCH	1.0	100 h	5	[19] *Nat. Commun.* **14**, 1822 (2023)
P/Fe-N-C	1.0	192 h	10	[30] *J. Am. Chem. Soc.***145**, 3647-3655 (2023)
Ru SAS/SNC	1.0	270 h	5	[34] *J. Am. Chem. Soc.* **144**, 2197-2207 (2022)
Fe-Co-Ni MOF	1.0	120 h	5	[33] *J. Am. Chem. Soc.* **144**, 3411-3428 (2022)
FeNC-V_N	film	980 h	5	[8] *J. Am. Chem. Soc.* **146**, 4803-4813 (2024)
FeCo-NPC	10	60 h	10	[20] *Adv. Mater.* **36**, 2306047 (2024)
Fe_H-N-C	1.0	1200 h	5	[37] *Adv. Mater.* **35**, 2210714 (2023)
VMoON@NC	2.0	630 h	10	[46] *Adv. Mater.* **35**, 2302625 (2023)
$CuCo_2O_{4-x}S_x$/NC-2	6.0	300 h	10	[47] *Adv. Mater.* **35**, 2370257 (2023)
Cu-Co/NC	1.0	510 h	10	[48] *Adv. Mater.* **35**, 2300905 (2023)
SA-Fe-SNC@900	2.0	160 h	5	[7] *Adv. Mater.* **35**, 2209948 (2023)
T-Fe SAC	4.0	350 h	20	[49] *Angew. Chem. Int. Ed.* **136**, e202319370 (2024)
Fe-SA/N-HCS	1.0	400 h	5	[50] *Angew. Chem. Int. Ed.* **135**, e202309784 (2023)
$ZnCo_2O_{4-x}F_x$/CNTs	6.0	300 h	5	[51] *Angew. Chem. Int. Ed.* **62**, e202301408 (2023)

Pd-Gd_2O_3/C+RuO_2	-	580 h	5	[42] *Angew. Chem. Int. Ed.* **62**, e202314565 (2023)
Fe_x/FeN_3S_1-C	1.0	600 h	5	[23] *Energy Environ. Sci.* **17**, 4746-4757 (2024)
Co-N-B-C	1.0	185 h	5	[12] *Energy Environ. Mater.* **7**, e12569 (2024)
FeSA/N-PSCS	2.0	150 h	10	[22] *Energy Storage Mater.* **59**, 102790 (2023)

Reference

[1] Dai-Yi, Q. & Zi, G. XPS study of tungsten carbide. *Chin. J. Chem*. **8**, 301-305 (1990).

[2] Zellner, M. B. & Chen, J. G. Surface science and electrochemical studies of WC and W_2C PVD films as potential electrocatalysts. *Catal. Today* **99**, 299-307 (2005).

[3] Nazon, J., Herbst, M., De Lucas, M. M., Bourgeois, S. & Domenichini, B. WC-based thin films obtained by reactive radio-frequency magnetron sputtering using W target and methane gas. *Thin Solid Films* **591**, 119-125 (2015).

[4] Zhang, H. L., Wang, D. Z., & Huang, N. K. The effect of nitrogen ion implantation on tungsten surfaces. *Appl. Surf. Sci*. **150**, 34-38 (1999).

[5] Martin, I., Vinatier, P., Levasseur, A., Dupin, J. C., & Gonbeau, D. XPS analysis of the lithium intercalation in amorphous tungsten oxysulfide thin films. *J. Power Sources* **81**, 306-311. (1999).

[6] Li, H. et al. Superstructure-assisted single-atom catalysis on tungsten carbides for bifunctional oxygen reactions. *J. Am. Chem. Soc*. **146**, 9124-9133. (2024).

[7] Chen, Z. et al. Mass production of sulfur-tuned single-atom catalysts for Zn-air batteries. *Adv. Mater*. **35**, 2209948. (2023).

[8] ul Haq, M. et al. Derived-2D $Nb_4C_3T_x$ sheets with interfacial self-assembled Fe-NC single-atom catalyst for electrocatalysis in water splitting and durable zinc-air battery. *Appl. Catal. B Environ*. **344**, 123632 (2024).

[9] Lyu, L. et al. Oxygen reduction kinetics of Fe-N-C single atom catalysts boosted by pyridinic N vacancy for temperature-adaptive Zn-Air batteries. *J. Am. Chem. Soc*. **146**, 4803-4813 (2024).

[10] Liu, J., Chen, W., Yuan, S., Liu, T., & Wang, Q. High-coordination Fe-N_4SP single-atom catalysts via the multi-shell synergistic effect for the enhanced oxygen reduction reaction of rechargeable Zn-air battery cathodes. *Energy & Environ. Sci.* **17**, 249-259 (2024).

[11] Yang, X. et al. A vacuum vapor deposition strategy to Fe single-atom catalysts with densely active sites for high-performance Zn-air battery. *Adv. Sci.* **11**, 2306594 (2024).

[12] Xu, C. et al. Boric acid-assisted pyrolysis for high-loading single-atom catalysts to boost oxygen reduction reaction in Zn-air batteries. *Energy & Environ. Mater*. **7**, e12569 (2024).

[13] Liu, H. et al. Microporous hard carbon support provokes exceptional performance of single atom electrocatalysts for advanced air cathodes. *Angew. Chem. Int. Ed*. e202501307 (2025).

[14] Liu, H. et al. Construction of single-atomic Fe and Cu sites within nitrogen/sulfur co-doped carbon matrix for boosting the performance of zinc-air batteries. *Appl. Catal. B Environ*. **362**, 124705 (2025).

[15] Zhao, Y. X. et al. A "pre-division metal clusters" strategy to mediate efficient dual-active sites ORR catalyst for ultralong rechargeable Zn-air battery. *Angew. Chem. Int. Ed*. **62**, e202216950 (2023).

[16] Zhang, L. et al. Coordination engineering and electronic structure modulation of FeNi dual-single-atoms encapsulated in N, P-codoped 3D hierarchically porous carbon electrocatalyst for synergistically boosting oxygen reduction reaction. *Appl. Catal. B Environ*. **351**, 123991 (2024).

[17] Lei, X. et al. High-entropy single-atom activated carbon catalysts for sustainable oxygen electrocatalysis. *Nat. Sustain*. **6**, 816-826 (2023).

[18] Yuan, Y. et al. Zirconium nitride catalysts surpass platinum for oxygen reduction. *Nat. Mater*. **19**, 282-286 (2020).

[19] Jiang, Z. et al. Interfacial assembly of binary atomic metal-N_x sites for high-performance energy devices. *Nat. Commun*. **14**, 1822 (2023).

[20] Pei, Z. et al. Atomically dispersed Fe sites regulated by adjacent single Co atoms anchored on N-P co-doped carbon structures for highly efficient oxygen reduction reaction. *Adv. Mater*. **36**, 2306047 (2024).

[21] Wu, Y. et al. Soft template-directed interlayer confinement synthesis of a Fe-Co dual single-atom catalyst for Zn-air batteries. *Energy Storage Mater.* **45**, 805-813 (2022).

[22] Shen, M. et al. Breaking the N-limitation with N-enriched porous submicron carbon spheres anchored Fe single-atom catalyst for superior oxygen reduction reaction and Zn-air batteries. *Energy Storage Mater.* **59**, 102790 (2023).

[23] Chen, J. et al. Wood-derived Fe cluster-reinforced asymmetric single-atom catalysts and weather-resistant organohydrogel for wide-temperature flexible Zn-air batteries. *Energy Environ. Sci.* **17**, 4746-4757 (2024).

[24] Sun, K. et al. $Co(CN)_3$ catalysts with well-defined coordination structure for the oxygen reduction reaction. *Nat. Catal.* **6**, 1164-1173 (2023).

[25] Shinde, S. S. et al. Ampere-hour-scale zinc–air pouch cells. *Nat. Energy* **6**, 592-604 (2021).

[26] Cheng, W. et al. Lattice-strained metal–organic-framework arrays for bifunctional oxygen electrocatalysis. *Nat. Energy* **4**, 115-122 (2019).
[27] Zhao, Y. et al. Few-layer graphdiyne doped with sp-hybridized nitrogen atoms at acetylenic sites for oxygen reduction electrocatalysis. *Nat. Chem.* **10**, 924-931 (2018).
[28] Rao, P. et al. Movable type printing method to synthesize high-entropy single-atom catalysts. *Nat. Commun.* **13**, 5071 (2022).
[29] Wang, Q. et al. Quasi-solid-state Zn-air batteries with an atomically dispersed cobalt electrocatalyst and organohydrogel electrolyte. *Nat. Commun.* **13**, 3689 (2022).
[30] Zhou, Y. et al. Boosting oxygen electrocatalytic activity of Fe–N–C catalysts by phosphorus incorporation. *J. Am. Chem. Soc.* **145**, 3647-3655 (2023).
[31] Zhao, Z. et al. Constructing unique mesoporous carbon superstructures via monomicelle interface confined assembly. *J. Am. Chem. Soc.* **144**, 11767-11777 (2022).
[32] Jiang, Y. et al. Linker-compensated metal-organic framework with electron delocalized metal sites for bifunctional oxygen electrocatalysis. *J. Am. Chem. Soc.* **144**, 4783-4791 (2022).
[33] Shahbazi Farahani, F. et al. Trilayer metal-organic frameworks as multifunctional electrocatalysts for energy conversion and storage applications. *J. Am. Chem. Soc.* **144**, 3411-3428 (2022).
[34] Qin, J. et al. Altering ligand fields in single-atom sites through second-shell anion modulation boosts the oxygen reduction reaction. *J. Am. Chem. Soc.* **144**, 2197-2207 (2022).
[35] Zhou, C. et al. Superdurable bifunctional oxygen electrocatalyst for high-performance zinc–air batteries. *J. Am. Chem. Soc.* **144**, 2694−2704 (2022).
[36] Ji, B. et al. Coordination chemistry of large-sized yttrium single-atom catalysts for oxygen reduction reaction. *Adv. Mater.* **35**, 2300381 (2023).
[37] Tian, H. et al. High durability of Fe–N–C single-atom catalysts with carbon vacancies toward the oxygen reduction reaction in alkaline media. *Adv. Mater.* **35**, 2210714 (2023).
[38] Yao, W. et al. Hierarchically ordered macro–mesoporous electrocatalyst with hydrophilic surface for efficient oxygen reduction reaction. *Adv. Mater.* **35**, 2301894 (2023).
[39] Huang, H. et al. Tailoring oxygen reduction reaction kinetics on perovskite oxides via oxygen vacancies for low-temperature and knittable zinc–air batteries. *Adv. Mater.* **35**, 2303109 (2023).
[40] You, Z. et al. Metal-free carbon-based covalent organic frameworks with heteroatom-free units boost efficient oxygen reduction. *Adv. Mater.* **35**, 2209129 (2023).
[41] Xie, Y. et al. Direct oxygen-oxygen cleavage through optimizing interatomic distances in dual single-atom electrocatalysts for efficient oxygen reduction reaction. *Angew. Chem. Int. Ed.* **135**, e202301833 (2023).
[42] Ning, S. et al. Importing antibonding-orbital occupancy through Pd−O−Gd bridge promotes electrocatalytic oxygen reduction. *Angew. Chem. Int. Ed.* **62**, e202314565 (2023).
[43] Tong, M. et al. Potential dominates structural recombination of single atom Mn sites for promoting oxygen reduction reaction. *Angew. Chem. Int. Ed.* **62**, e202314933 (2023).
[44] Luo, M. et al. PdMo bimetallene for oxygen reduction catalysis. *Nature* **574**, 81-85 (2019).
[45] Li, Y. et al. Main-group element-boosted oxygen electrocatalysis of Cu-N-C sites for zinc-air battery with cycling over 5000 h. *Nat. Commun.* **15**, 8365 (2024).
[46] Balamurugan, J. et al. Electrocatalysts for zinc–air batteries featuring single molybdenum atoms in a nitrogen-doped carbon framework. *Adv. Mater.* **35**, 2302625 (2023).
[47] Cai, J. et al. Hetero-anionic structure activated Co-S bonds promote oxygen electrocatalytic activity for high-efficiency zinc-air batteries. *Adv. Mater.* **35**, 2370257 (2023).
[48] Li, Z. et al. Geometric and electronic engineering of atomically dispersed copper-cobalt diatomic sites for synergistic promotion of bifunctional oxygen electrocatalysis in zinc–air batteries. *Adv. Mater.* **35**, 2300905 (2023).
[49] Zhu, Y. et al. Tip-like Fe-N_4 sites induced surface microenvironments regulation boosts the oxygen reduction reaction. *Angew. Chem. Int. Ed.* **136**, e202319370 (2024).
[50] Zong, L. et al. Constructing Fe-N_4 sites through anion exchange-mediated transformation of Fe coordination environments in hierarchical carbon support for efficient oxygen reduction. *Angew. Chem. Int. Ed.* **135**, e202309784 (2023).

[51] Xiao, K., Wang, Y., Wu, P., Hou, L., & Liu, Z. Q. Activating lattice oxygen in spinel $ZnCo_2O_4$ through filling oxygen vacancies with fluorine for electrocatalytic oxygen evolution. *Angew. Chem. Int. Ed.* **62**, e202301408 (2023).